

Inadequate turbulent support in low-metallicity molecular clouds

Lingrui Lin^{1,2}, Zhi-Yu Zhang^{1,2,*}, Junzhi Wang^{3,*}, Padelis P. Papadopoulos^{4,5}, Yong Shi^{1,2}, Yan Gong^{6,7}, Yan Sun⁷, Yichen Sun^{1,2}, Thomas G. Bisbas⁸, Donatella Romano⁹, Di Li^{10,11,12}, Haoyu Baobab Liu^{13,14}, Keping Qiu^{1,2}, Lijie Liu^{15,16,17}, Gan Luo^{1,2,18}, Chao-Wei Tsai^{11,19,20}, Jingwen Wu^{11,20}, Siyi Feng²¹, and Bo Zhang²²

¹School of Astronomy and Space Science, Nanjing University, Nanjing 210093, China

²Key Laboratory of Modern Astronomy and Astrophysics (Nanjing University), Ministry of Education, Nanjing 210093, China

³Guangxi Key Laboratory for Relativistic Astrophysics, School of Physical Science and Technology, Guangxi University, Nanning 530004, China

⁴Department of Physics, Section of Astrophysics, Astronomy and Mechanics, Aristotle University of Thessaloniki, 54124 Thessaloniki, Greece

⁵Research Center for Astronomy, Academy of Athens, Soranou Efessiou 4, GR-11527, Athens, Greece

⁶Max-Planck-Institut für Radioastronomie, Auf dem Hügel 69, D-53121 Bonn, Germany

⁷Purple Mountain Observatory and Key Laboratory of Radio Astronomy, Chinese Academy of Sciences, Nanjing 210008, China

⁸Research Center for Astronomical Computing, Zhejiang Laboratory, Hangzhou 311100, China

⁹INAF, Astrophysics and Space Science Observatory, Via Gobetti 93/3, I-40129 Bologna, Italy

¹⁰Department of Astronomy, Tsinghua University, Beijing 100084, China

¹¹National Astronomical Observatories, Chinese Academy of Sciences, A20 Datun Road, Chaoyang District, Beijing 100101, China

¹²Zhejiang Lab, Hangzhou, Zhejiang 311121, People's Republic of China

¹³Department of Physics, National Sun Yat-Sen University, No. 70, Lien-Hai Road, Kaohsiung City 80424, Taiwan

¹⁴Center of Astronomy and Gravitation, National Taiwan Normal University, Taipei 116, Taiwan

¹⁵Cosmic Dawn Center (DAWN), Copenhagen, Denmark

¹⁶Niels Bohr Institute, University of Copenhagen, Lyngbyvej 2, 2100 Copenhagen Ø, Denmark

¹⁷DTU-Space, Technical University of Denmark, Elektrovej 327, DK2800 Kgs. Lyngby, Denmark

¹⁸Institut de Radioastronomie Millimétrique, 300 rue de la Piscine, Domaine Universitaire de Grenoble, F-38406 Saint-Martin d'Hères, France

¹⁹Institute for Frontiers in Astronomy and Astrophysics, Beijing Normal University, Beijing 102206, China

²⁰School of Astronomy and Space Science, University of Chinese Academy of Sciences, Beijing 100049, China

²¹Department of Astronomy, Xiamen University, Zengcuo'an West Road, Xiamen, 361005, China

²²Shanghai Astronomical Observatory, Chinese Academy of Sciences, 80 Nandan Road, Shanghai 200030, China

*corresponding author, z Zhang@nju.edu.cn, junzhiwang@gxu.edu.cn

ABSTRACT

The dynamic properties of molecular clouds are set by the interplay of their self-gravity, turbulence, external pressure and magnetic fields. Extended surveys of Galactic molecular clouds typically find that their kinetic energy (E_k) counterbalances their self-gravitational energy (E_g), setting their virial parameter $\alpha_{\text{vir}} = 2E_k/|E_g| \approx 1$. However, past studies either have been biased by the use of optically-thick lines or have been limited within the solar neighborhood and the inner Galaxy (Galactocentric radius $R_{\text{gc}} < R_{\text{gc},\odot} \approx 8$ kpc). Here we present sensitive mapping observations of optically thin ^{13}CO lines towards molecular clouds in the low-metallicity Galactic outer disk ($R_{\text{gc}} \sim 9 - 24$ kpc). By combining archival data from the inner Galaxy and four nearby metal-poor dwarf galaxies, we reveal a systematic trend of α_{vir} , which declines from supervirial dynamic states in metal-rich clouds to extremely subvirial dynamic states in metal-poor clouds. In these metal-poor environments, turbulence alone is insufficient to counterbalance the self-gravity of a cloud. A cloud-volumetric magnetic field may replace turbulence as the dominant cloud-supporting mechanism in low-metallicity conditions, for example, the outermost galactic disks, dwarf galaxies and galaxies in the early Universe, which would then inevitably impact the initial conditions for star formation in such environments.

Larson's relations¹ have been well established both in the Milky Way¹⁻⁴ and in external galaxies⁵⁻¹⁰. They consist of power-law relations among the size, velocity dispersion, and mass of molecular clouds. Such relations are often considered as the outcome of virial equilibrium^{1,11} (or energy equipartition¹²; Methods) between the turbulent kinetic energy (E_k) and the self-gravitational energy (E_g) of a molecular cloud, which is characterized by the virial parameter ($\alpha_{\text{vir}} = 2E_k/|E_g|$)¹³ that is typically near unity¹⁻³. Molecular clouds resolved in the Galactic Centre and in some external galaxies seem to have a slight preference towards supervirial states ($\alpha_{\text{vir}} > 1$), possibly due to external pressure on cloud boundaries¹⁴ or tidal shear around the cloud envelopes¹⁵⁻¹⁷. The virial equilibrium assumption has been used in a variety of contexts, such as for calibrating the standard value of the so-called CO-to- H_2 conversion factor (X_{CO})¹⁸, for estimating the average turbulent gas pressure in high-redshift galaxies¹⁹ and for setting the initial conditions of star formation in numerical simulations^{20,21}.

Nevertheless, most previous studies on the dynamic states of molecular clouds were based solely on the more luminous but optically thick low- J ^{12}CO transitions^{2,4}. The uncertainty of X_{CO} values¹⁸, the opacity broadening²² and the radiative trapping of ^{12}CO lines (Methods; the latter can keep ^{12}CO lines luminous even for low-density outer-cloud envelope gas, which may not be gravitationally bound) undoubtedly complicate α_{vir} estimates for molecular clouds.

Rotational transitions of the rarer ^{13}CO molecule²³, on the other hand, are optically thin for the bulk of the mass in molecular clouds in most cases²⁴. Therefore, the low- J ^{13}CO lines can more faithfully trace H_2 mass and velocity dispersion³ than the ^{12}CO lines. However, because of their faintness, studies of cloud dynamics based on ^{13}CO lines are mostly limited to within a Galactocentric radius (R_{gc}) of less than 12 kpc (refs. 25, 26), which includes the solar neighbourhood¹ and the inner Galaxy^{3,27,28} but leaves the Galactic outer disk less explored.

The Galactic outer disk, namely, the portion of the disk beyond the solar circle ($R_{\text{gc}} > R_{\text{gc},\odot} \approx 8$ kpc)²⁹, features very different physical conditions, such as low midplane pressure³⁰, a low turbulence injection level⁴ and low gas-phase metallicity (Z , routinely traced by the oxygen abundance, O/H)³¹. Such environments reflect not only the early formation stage of the Galactic thin disk³² but also the general properties of gas-rich, metal-poor galaxies^{33,34}.

In this work, we performed mapping observations of the ^{13}CO $J = 1 \rightarrow 0$ and $J = 2 \rightarrow 1$ transitions for a sample of molecular clouds in the Galactic outer disk ($9 < R_{\text{gc}} < 25$ kpc), using the Institut de

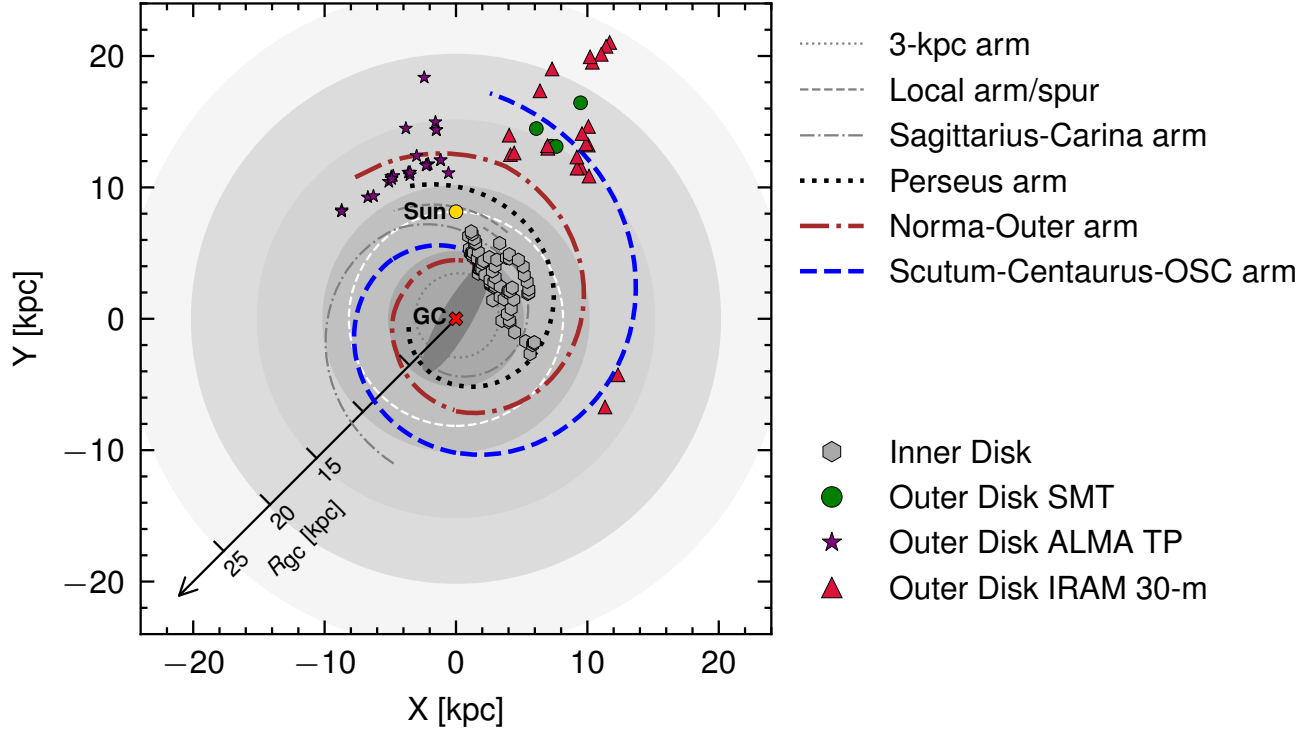


Fig. 1. Distribution of molecular clouds on the Galactic plane. Spiral arm models from the Bar and Spiral Structure Legacy (BeSSeL) Survey³⁶ are overlaid, including the 3-kpc arm (gray dotted line), the Local arm/spur (gray dashed line), the Sagittarius–Carina arm (gray dash-dotted line), the Perseus arm (black thick dotted line), the Norma–Outer arm (brown thick dash-dotted line), and the Scutum–Centaurus–OSC arm (blue thick dashed line). The gold dot and the red cross locate the Sun and the Galactic center (GC), respectively. The white dashed line shows the Solar circle ($R_{\text{gc},\odot}$). The gray-shadowed regions represent Galactocentric radii of 5, 10, 15, 20, and 25 kpc. Purple stars, red triangles, and green dots are the outer disk molecular clouds observed with ALMA Total Power, IRAM 30-m, and SMT, respectively. The gray hexagons show inner disk molecular clouds from the Galactic Ring Survey³.

radioastronomie millimétrique (IRAM) 30 m telescope, the single-dish telescope (Total Power (TP) Array) of the Atacama Large Millimeter/submillimeter Array (ALMA) and the Submillimeter Telescope (SMT). Figure 1 shows the spatial distribution of our samples on the Galactic plane.

We first derived the surface density of ^{13}CO ($N_{^{13}\text{CO}}$) from the ^{13}CO emission and then obtained the H_2 surface density (N_{H_2}) with the $\text{H}_2/^{13}\text{CO}$ abundance ratio estimated from the Galactic radial gradients of $^{12}\text{C}/^{13}\text{C}$ (ref. 35) and O/H (ref. 31; Methods). For each cloud, we measured the equivalent cloud radius (R_{cloud}), the velocity dispersion (σ_v) and the molecular gas mass (M_{mol}), all within the half-peak isophote of N_{H_2} (Methods). Cloud distances were estimated based on the Galactic rotation curve model from the Bar and Spiral Structure Legacy (BeSSeL) survey³⁶.

For comparison, we retrieved archival $^{13}\text{CO } J = 1 \rightarrow 0$ and $J = 2 \rightarrow 1$ data from the inner Galaxy³ and nearby metal-poor dwarf galaxies, namely, the Large Magellanic Cloud⁹ (LMC; $Z \approx 0.5 Z_{\odot}$; ref. 37), the Small Magellanic Cloud³⁸ (SMC; $Z \approx 0.2 Z_{\odot}$; ref. 39) and NGC 6822 ($Z \approx 0.2 Z_{\odot}$)⁴⁰. We also took the physical properties of molecular clumps from an extremely metal-poor dwarf galaxy DDO 70 ($Z \approx 0.07 Z_{\odot}$) from the literature⁴¹.

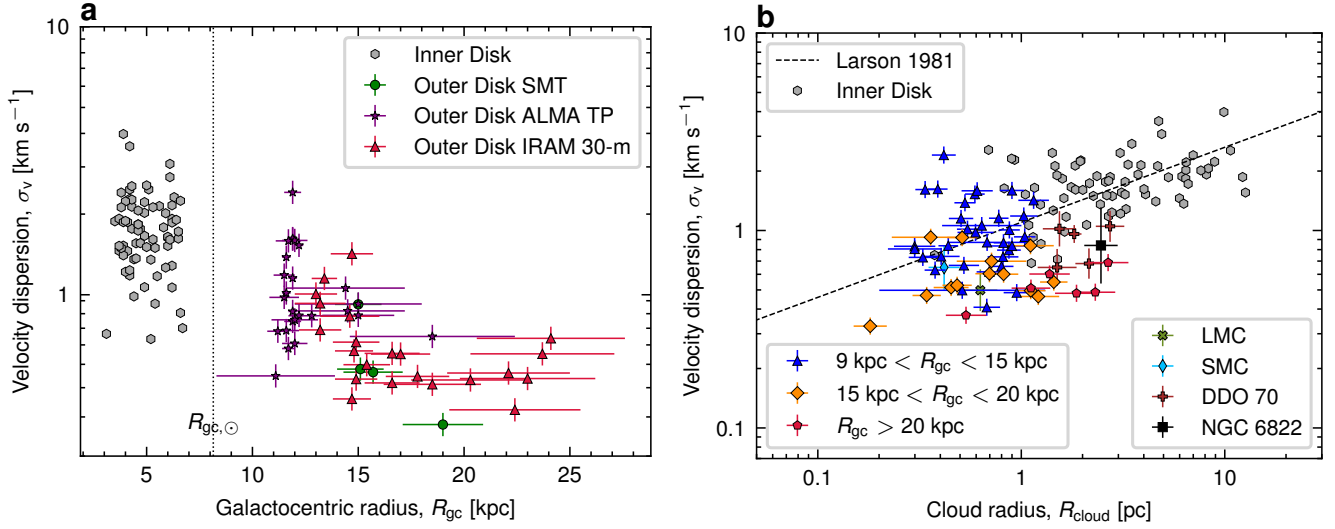


Fig. 2. Variations of the cloud velocity dispersion. **a**, σ_v versus R_{gc} . Purple stars, red triangles, and green dots are the outer disk molecular clouds observed with ALMA Total Power, IRAM 30-m, and SMT, respectively. The gray hexagons show inner disk molecular clouds from the Galactic Ring Survey³. The vertical black-dotted line shows the Galactocentric radius of the Sun ($R_{\text{gc}, \odot}$). **b**, σ_v versus R_{cloud} . The outer disk molecular clouds are divided into three R_{gc} bins: $9 \text{ kpc} < R_{\text{gc}} < 15 \text{ kpc}$ (blue triangles), $15 \text{ kpc} < R_{\text{gc}} < 20 \text{ kpc}$ (orange diamonds), and $R_{\text{gc}} > 20 \text{ kpc}$ (red pentagons). Molecular clouds from metal-poor galaxies, i.e. LMC (olive cross, median), SMC (blue thin-diamond, median), NGC 6822 (black squares, median) and DDO 70 (brown pluses), are overlaid. The dashed line shows the classical Larson’s $\sigma_v - R_{\text{cloud}}$ relation¹. Data are presented as measured values with 1- σ uncertainties.

Figure 2a shows that the velocity dispersion σ_v of the Galactic molecular clouds decreases from $R_{\text{gc}} = 5 \text{ kpc}$ to 15 kpc , with this trend becoming flat at $R_{\text{gc}} > 15 \text{ kpc}$. This is consistent with the results from a low-resolution $^{12}\text{CO } J = 1 \approx 0$ survey on a tens of parsecs scale⁴ and may be related to the decreasing kinetic energy injection towards the outer Galaxy (Methods). Figure 2b presents σ_v versus R_{cloud} , showing that, although molecular clouds at $R_{\text{gc}} < 15 \text{ kpc}$ roughly follow the classical Larson’s σ_v versus R_{cloud} relation¹, those at $R_{\text{gc}} > 15 \text{ kpc}$ and those from metal-poor dwarf galaxies have a lower σ_v than what would be expected from Larson’s relation. Such a discrepancy has also been revealed by ^{12}CO line observations of metal-poor dwarf galaxies, including the Magellanic Clouds^{5,42}.

Figure 3 shows that the α_{vir} of molecular clouds, from both the Milky Way and metal-poor dwarf galaxies, systematically varies as a function of the gas-phase metallicity. The gas-phase metallicities of the Galactic clouds were estimated using the Galactic radial gradient of O/H (ref. 31). α_{vir} decreases from supvirial states ($\alpha_{\text{vir}} > 1$) in the metal-rich inner Galaxy to subvirial states ($\alpha_{\text{vir}} < 1$) towards the metal-poor outer Galaxy with $R_{\text{gc}} > 15 \text{ kpc}$ ($Z < 0.5 Z_{\odot}$). The slope of this correlation is sensitive to the adopted $\text{H}_2/^{13}\text{CO}$ abundance ratio gradient. Nevertheless, the overall trend is robust due to the monotonically decreasing Galactic radial gradients for both $^{12}\text{C}/^{13}\text{C}$ and the gas-phase metallicity. Molecular clouds from metal-poor dwarf galaxies, that is, the LMC ($Z \approx 0.5 Z_{\odot}$)³⁷, the SMC ($Z \approx 0.2 Z_{\odot}$)³⁹, NGC 6822 ($Z \approx 0.2 Z_{\odot}$)⁴⁰ and DDO 70 ($Z \sim 0.07 Z_{\odot}$)⁴¹, extend the α_{vir} versus Z trend to the extremely low-metallicity end, despite that these systems have a variety of stellar contents, star-formation properties and galactic dynamic conditions. Consequently, we found that the classical virial equilibrium between E_k and E_g of molecular clouds is not universal.

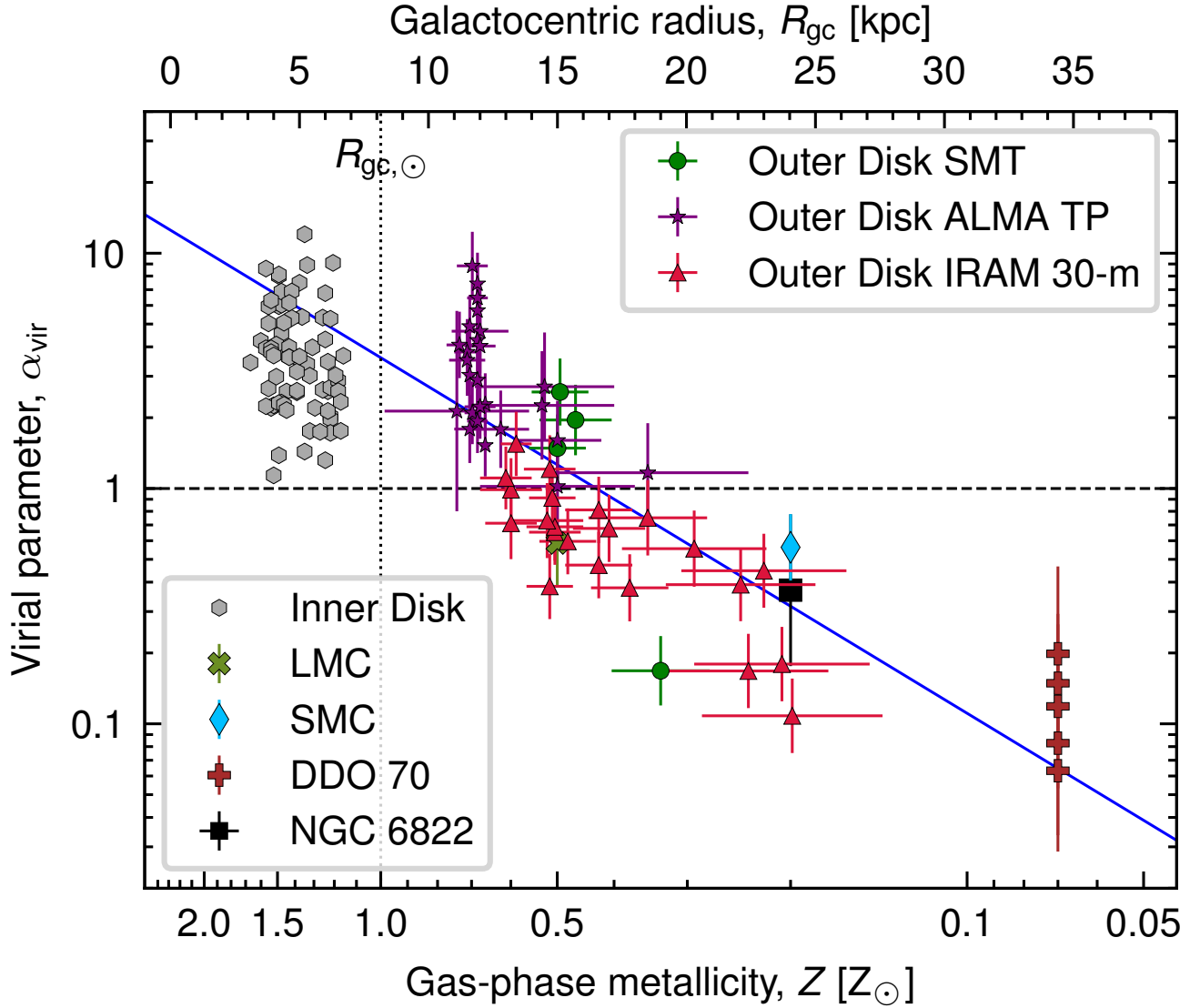


Fig. 3. Variation of cloud virial parameter as a function of the gas-phase metallicity. Purple stars, red triangles, and green dots are the outer disk molecular clouds observed with ALMA Total Power, IRAM 30-m, and SMT, respectively. The gray hexagons show inner disk molecular clouds from the Galactic Ring Survey³. Molecular clouds from metal-poor galaxies, i.e. LMC (olive cross, median), SMC (blue thin-diamond, median), NGC 6822 (black squares, median) and DDO 70 (brown pluses), are overlaid. The black-dashed line represents the virial equilibrium between the kinetic energy and the self-gravitational energy, namely $\alpha_{\text{vir}} = 1$. The vertical black dotted line shows the Galactocentric radius of the Sun ($R_{\text{gc},\odot}$). For molecular clouds in the Milky Way, the gas-phase metallicity (Z , bottom axis) is estimated from the Galactocentric radius (R_{gc} , top axis) through the O/H- R_{gc} gradient³¹. The blue line shows a linear fitting of the $\alpha_{\text{vir}}-Z$ trend using the ^{13}CO data in the Milky Way (see Methods). Data are presented as measured values with $1-\sigma$ uncertainties.

Although by definition α_{vir} includes only E_k and E_g , the general virial theorem^{11,13,43} (Methods) also contains terms dependent on the volumetric magnetic field (B) and the cloud-boundary pressure (P_c). These other mechanisms can support and confine molecular clouds, respectively^{11,13}.

The subvirial clouds found at $Z < 0.5 Z_{\odot}$ ($R_{\text{gc}} > 15$ kpc) indicate that the turbulent velocity fields alone are not sufficient to counterbalance the cloud self-gravity in such low-metallicity conditions. To sustain the survival of the clouds, another mechanism is necessary. The most plausible mechanism appears to be the magnetic field (Methods).

Using the general virial theorem and assuming efficient momentum transfer between ions and neutral species⁴⁴, we found that the B -field strengths required to support subvirial clouds are consistent with expectations. These are based on the B versus n_{H} relation benchmarked in the solar neighborhood and the inner Galaxy⁴⁵ (n_{H} , volume density of hydrogen nuclei; Methods). Therefore, the subvirial clouds in metal-poor conditions do not require a stronger B field than those in the metal-rich inner Galaxy. At low metallicities, the same B -field strength can overtake turbulence in balancing the self-gravity of a cloud.

The conditions necessary for such subvirial states may arise from the distinct physical properties typical of low-metallicity environments (Methods). These include reduced turbulence in atomic gas⁴⁶ and a higher ionization fraction in molecular gas. The latter would enhance the coupling between B -field lines and gas⁴⁷, allowing the magnetic field to play a more dominant role in counteracting self-gravity compared to high-metallicity regimes.

The supervirial molecular clouds from the metal-rich inner Galaxy, on the other hand, are probably the result of enhanced gas pressures at cloud boundaries ($P_{\text{e}}/k \approx 10^4 - 10^7$ K cm⁻³), as previously proposed in the literature⁴⁸. Other factors, such as cloud-boundary magnetic fields, tidal effects¹⁵⁻¹⁷ and even embedded stellar objects⁴⁹, can all drive α_{vir} above unity (Methods).

Regardless of the detailed mechanisms driving the supervirial and subvirial conditions, the dynamic states of molecular clouds seem to depend strongly on the ambient environments. This will inevitably impact all star formation theories, given that the dynamic states of molecular clouds are crucial aspects of the initial conditions for star formation in galaxies. The subvirial states found in low- Z molecular clouds, in particular, are expected to be consequential for star formation in several environments, such as the outskirts of main-sequence galaxies (still metal-poor), dwarf galaxies and galaxies at cosmic dawn⁵⁰.

Methods

Observations towards the Galactic outer disk clouds

• **IRAM 30 m telescope observations.** Observations with the IRAM 30 m telescope were executed from 29 August to 5 September 2017 (Project ID 031-17, principal investigator (PI) Z.-Y. Zhang) and from 3 to 30 January 2023 (Project ID 102-22, PI T. Bisbas). The targets were selected from the literature⁵¹⁻⁵⁴, based on both their ¹²CO brightness and Galactocentric radius.

In Project 031-17, we performed on-the-fly (OTF) mapping observations towards 14 molecular clouds in the outer Galactic disk. We used the Eight MIXer Receiver (EMIR) at 3 mm (E0), which was equipped with the fast Fourier transform spectrometer in FTS200 mode, to target the ¹³CO $J = 1 \rightarrow 0$ transition. The spectral resolution was 195 kHz, corresponding to a velocity resolution of ~ 0.53 km s⁻¹ at the rest frequency of ¹³CO $J = 1 \rightarrow 0$ (110.20135430 GHz). The mapping area towards each target was $2.5' \times 2.5'$ along both right ascension and declination. The step between each OTF scan of rows and columns was $9''$, and the separation between each integration was $4.8''$, enabling a super-Nyquist sampling of the half power beam-width ($\theta_{\text{beam}} \approx 23.5''$).

The OTF mapping data were reduced with GILDAS/CLASS. Platforming effects were firstly removed by separately fitting and subtracting the baselines of each FTS200 unit. We extracted a velocity interval centred at the ¹³CO $J = 1 \rightarrow 0$ line with a width of ~ 18 times the full width of half maximum linewidth. We used the xy_map task to build regular ¹³CO spectral cubes with pixel sizes of $4'' \times 4''$. Given a main beam efficiency (η_{beam}) of 0.78 (<https://publicwiki.iram.es/Iram30mEfficiencies>),

the typical root-mean-square (r.m.s.) main beam temperature ($T_{\text{mb,rms}}$) was ~ 0.13 K.

In Project 102-22, we mapped ten outer disk molecular clouds, covering the $J = 1 \rightarrow 0$ lines of ^{12}CO and ^{13}CO using the E0 receiver. The step between each OTF scan of rows and columns was $4.5''$ and the separation between each integration was $2.6''$. We reduced the data and built the spectral cubes following the same procedure used for Project 031-17. The typical $T_{\text{mb,rms}} \approx 0.08$ K. Two of the ten targets were excluded in this work due to their low signal-to-noise ratio (S/N).

• **ALMA TP Array observations.** The ALMA observations (Project ID 2021.2.00175.S, PI L. Lin) were executed during ALMA cycle 8 from 29 January to 28 September 2022. The $J = 2 \rightarrow 1$ transitions of ^{12}CO and ^{13}CO were covered. The targets were selected from the literature⁵¹. We obtained $4' \times 4'$ OTF maps towards 26 outer-disk molecular clouds in the third Galactic quadrant ($180^\circ < l < 270^\circ$ where l is the Galactic longitude) with the ALMA TP Array. The data were reduced with the standard pipeline. The θ_{beam} and the velocity resolution at the rest frequency of $^{13}\text{CO } J = 2 \rightarrow 1$ (220.39868420 GHz) were $\sim 29.5''$ and 0.16 km s^{-1} , respectively. The typical $T_{\text{mb,rms}} \approx 0.04$ K.

• **SMT observations.** The SMT observations (Project ID Lin_L_22B_1, PI L. Lin) were executed from 29 October to 1 November 2022. We obtained $4' \times 4'$ OTF maps towards 13 outer-disk molecular clouds^{51,52}, nine of which had $^{13}\text{CO } J = 1 \rightarrow 0$ observations made by IRAM 30 m telescope. Therefore, only four targets are included in this work. The $J = 2 \rightarrow 1$ transitions of ^{12}CO and ^{13}CO were covered. The step between each OTF scan of rows/columns was $10''$, and the separation between each integration was $\sim 1.3''$, enabling a super-Nyquist sampling of $\theta_{\text{beam}} \approx 36''$. The velocity resolution was 0.34 km s^{-1} . Given $\eta_{\text{beam}} = 0.70$, the typical $T_{\text{mb,rms}} \approx 0.14$ K.

The numbers of molecular clouds observed by us at $9 \text{ kpc} \leq R_{\text{gc}} < 15 \text{ kpc}$, $15 \text{ kpc} \leq R_{\text{gc}} < 20 \text{ kpc}$, and $R_{\text{gc}} \geq 20 \text{ kpc}$ are 33, 13, and six, respectively.

Archival data

• **Galactic Ring Survey $^{13}\text{CO } J = 1 \rightarrow 0$ data from the inner Galaxy.** We retrieved the $^{13}\text{CO } J = 1 \rightarrow 0$ data for a sample of inner disk molecular clouds³ studied by the Galactic Ring Survey (GRS)⁵⁵. The spatial sampling step of GRS was $22''$, enabling a Nyquist sampling of the telescope beam ($\theta_{\text{beam}} = 46''$)⁵⁵. Given a main beam efficiency $\eta_{\text{mb}} = 0.46$, the typical r.m.s. main beam temperature is 0.27 K at the velocity resolution of 0.21 km s^{-1} . We visually excluded clouds suffering from severe line-of-sight (LoS) cloud blending. Our measurements are consistent with previous work³.

• **ALMA archival data of nearby galaxies.** With the capability of the ALMA 12-m array, molecular clouds in the nearby galaxies can be resolved on parsec scales.

▷ **LMC.** We used the ^{13}CO cubes provided in the literature⁹ for several regions in the LMC. Specifically, we included the $^{13}\text{CO } J = 1 \rightarrow 0$ cubes (ALMA 12 m only) for N59C, A439, GMC104 and GMC1, and the $^{13}\text{CO } J = 2 \rightarrow 1$ cube (ALMA 12 m plus the TP Array) for the Planck cold cloud. All cubes have a restored $\theta_{\text{beam}} = 3.5''$, corresponding to a physical resolution of 0.8 pc at the distance of the LMC. The r.m.s noise of the brightness temperature was ~ 0.2 K at a velocity resolution of 0.2 km s^{-1} .

▷ **SMC.** We retrieved ALMA $^{13}\text{CO } J = 2 \rightarrow 1$ data from the ALMA archival system (Project IDs 2013.1.00652.S and 2015.1.00581.S)³⁸. Four regions in the SMC (N22, SWBarN, SWBarS and SWDarkPK) were observed using the Atacama Compact Array (7 m array plus the TP Array; 2013.1.00652.S) and the ALMA 12 m array (2015.1.00581.S). The interferometry data (12 m plus 7 m arrays) were calibrated with the CASA pipeline (v4.5.2-r36115 and v4.2.2-r30986). The imaging was done by `tclean` in CASA v6.5.3. The ideal angular resolution of these observations

was $\sim 1''$. For consistency, however, we imaged the interferometry data with *weighting* = ‘*briggs*’ (*robust* = 2.0), *cell* = 0.4'' and *restoringbeam* = 2.0''. The channel width of the cleaned cubes was 0.2 km s⁻¹. The interferometry cubes were combined with the product TP cubes using the *feather* task. The typical r.m.s. brightness temperature was ~ 0.4 K (~ 0.06 Jy per beam).

- ▷ **NGC 6822.** For NGC 6822, we retrieved the ¹³CO $J = 1 \rightarrow 0$ data observed by ALMA 12 m array (Project ID 2019.1.01641.S). We calibrated the data with the standard CASA pipeline. The imaging was done by `tclean` in CASA v6.5.3. For a compromise between angular resolution and sensitivity, we imaged the data with *weighting* = ‘*briggs*’ (*robust* = 2.0), *cell* = 0.3'' and *restoringbeam* = 2.4''. The channel width was ~ 2.7 km s⁻¹. The typical r.m.s. brightness temperature was ~ 0.01 K (~ 0.6 mJy per beam).

We visually identified molecular clouds in the LMC, SMC and NGC 6822. To exclude clouds that were mixed with several components along the LoS, we kept only those isolated clouds for which the half-peak isophote of N_{H_2} was a single closed contour. Clouds with radii smaller than half of the resolution beam were excluded.

- ▷ **DDO 70.** We included five molecular clumps detected in a local extremely metal-poor galaxy, DDO 70 ($Z \approx 0.07 Z_{\odot}$, at a distance of 1.38 Mpc)⁴¹. Even though these clouds were identified through the ¹²CO $J = 2 \rightarrow 1$ emission, the cloud properties were measured independently of the uncertain X_{CO} (ref.⁴¹).

Supplementary Table 1 summarizes the details of the above new observations and archival data.

Supplementary Table 1: Information about the cloud samples. R_{gc} : Galactocentric radius; Z : gas-phase metallicity; ΔV_{ins} : instrumental broadening, i.e., channel width; θ_{beam} : half-power beam width; $T_{\text{b,rms}}$: root-mean-square noise of main beam temperature; Phy. Res.: physical resolution.

Location	R_{gc} (kpc)	Z (Z_{\odot})	¹³ CO transition ($J \rightarrow J - 1$)	Number	ΔV_{ins} (km s ⁻¹)	θ_{beam} ('')	$T_{\text{b,rms}}$ (K)	Phy. Res. (pc)
Outer Galaxy ^a	12.2 - 24.0	0.2 - 0.7	1 \rightarrow 0	14	0.53	23.5	0.13	0.56 - 2.0
Outer Galaxy ^b	16.1 - 23.0	0.2 - 0.4	1 \rightarrow 0	8	0.53	23.5	0.08	1.1 - 1.9
Outer Galaxy ^c	9.8 - 17.8	0.4 - 0.8	2 \rightarrow 1	26	0.16	29.5	0.04	0.24 - 1.4
Outer Galaxy ^d	15.7 - 16.6	0.4 - 0.5	2 \rightarrow 1	4	0.34	36.0	0.14	1.7 - 1.8
Inner Galaxy ^e	3.2 - 7.4	1.1 - 1.7	1 \rightarrow 0	72	0.21	46.0	0.27	0.56 - 2.0
LMC ^f	—	0.5	1 \rightarrow 0/2 \rightarrow 1	62	0.20/0.50	3.5	0.2	0.85
SMC ^g	—	0.2	2 \rightarrow 1	37	0.20	2.0	0.6	0.60
NGC 6822 ^h	—	0.2	1 \rightarrow 0	6	2.7	2.4	0.01	5.5
DDO 70 ⁱ	—	0.07	—	5	0.4	0.2	0.5	1.47

^a IRAM 30-m (2017), ^b IRAM 30-m (2023), ^c ALMA Total Power (Cycle 8), ^d SMT (2022), ^e FCRAO 14-m (The Galactic Ring Survey)^{3,55}, ^f ALMA 12-m/7-m/Total Power LMC⁹, ^g ALMA 12-m/7-m/Total Power SMC³⁸, ^h ALMA 12-m, ⁱ ALMA 12-m⁴¹

Distances and Galactocentric radii

We derived the heliocentric distances (d) and Galactocentric radii (R_{gc}) of the Galactic molecular clouds using the code provided by the BeSSeL survey³⁶. The Galactic rotation curve and spiral arm models were produced by measuring the trigonometric parallaxes and proper motions of ~ 200 molecular masers from the BeSSeL and the Japanese VLBI (very-long-baseline interferometry) Exploration of Radio Astrometry

project. All Galactic molecular clouds studied in this work are close to the Galactic plane (Galactic latitude $|b| < 4^\circ$), so the heights from the Galactic plane were negligible. The Galactocentric radius is, therefore, given by

$$R_{\text{gc}} = \sqrt{R_{\text{gc}, \odot}^2 + d^2 - 2R_{\text{gc}, \odot}d\cos(l)}, \quad (1)$$

where $R_{\text{gc}, \odot} = 8.15$ kpc is the Galactocentric radius of the Sun³⁶.

The inputs for the code are the Galactic longitude (l), Galactic latitude (b) and the local standard of rest velocity (V_{LSR}). The code calculates the probability density function (PDF) of cloud distance through a Bayesian approach ('Data Availability'), from which the heliocentric distances (d) and their uncertainties were inferred. For each cloud, we used the most probable distance and the associated error given by the Bayesian inference.

The PDF for the cloud distance was calculated by multiplying PDFs of (1) the association with a spiral arm model, (2) the kinematic distance from the rotation curve and (3) the vicinity to parallax sources. Each of these was weighted to construct the final PDF. However, because the spiral arm model in the far outer Galaxy ($R_{\text{gc}} \gtrsim 15$ kpc) was poorly constrained³⁶, we excluded the spiral arm model for all Galactic molecular clouds. Our results were not influenced, regardless of whether the spiral arm models were implemented. For most outer-disk clouds, there were no nearby parallax sources. Consequently, we adopted their kinematic distances based on the Galactic rotation curve.

For molecular clouds in the LMC, the SMC and NGC 6822, we adopted $d_{\text{LMC}} = 49.59 \pm 0.63$ kpc (ref. 56), $d_{\text{SMC}} = 62.44 \pm 1.28$ kpc (ref. 57), and $d_{\text{NGC 6822}} = 474 \pm 13$ kpc (ref. 58), respectively.

H₂ surface density

We first generated source masks for each spectral cube using the source-finding algorithm embedded in 3D BAROLO (ref. 59, 60). For molecular clouds in the Galactic outer disk as well as the LMC, the SMC and NGC 6822, we set MASK=Search, SNRCUT=3 and GROWTHCUT=2.5. Using this setting, signals in the line cube with $S/N > 3$ were iteratively identified as real emission. Then, the source mask was grown to include surrounding signals with $S/N > 2.5$. The data from the GRS for molecular clouds do not have enough line-free channels to estimate the spectral noise due to severe cloud blending. Therefore, we set THRESHOLD=0.39 and GROWTHTHRESHOLD=0.33. With this setting, the algorithm searches for values larger than 0.39 K ($S/N = 3$ in antenna temperature (T_{A}^*)) and growth to 0.33 K ($S/N = 2.5$ in T_{A}^*)⁵⁵ in the line cube.

We calculated the surface density of ¹³CO ($N_{13\text{CO}}$) under the assumption of local thermodynamic equilibrium (LTE). For molecular clouds with complementary ¹²CO data, we estimated the excitation temperature (T_{ex}) by assuming (1) that the low- J ¹³CO lines share the same T_{ex} with the ¹²CO lines and (2) that the ¹²CO lines are optically thick. Therefore, T_{ex} is related to the peak main beam temperature of the ¹²CO line ($T_{12, \text{pk}}$) through

$$J(T_{\text{ex}}, \nu) = f_{\text{bm}}^{-1} T_{12, \text{pk}} + J(T_{\text{bg}}, \nu), \quad (2)$$

where ν is the rest frequency of the line. The background temperature (T_{bg}) was taken as the brightness temperature of the cosmic microwave background ($T_{\text{CMB}} = 2.73$ K). The beam filling factor (f_{bm}) was assumed to be unity. $J(T, \nu)$ is the Rayleigh-Jeans Equivalent Temperature⁶¹:

$$J(T, \nu) \equiv \frac{h\nu/k}{\exp(h\nu/kT) - 1}. \quad (3)$$

where k is the Boltzmann constant and h is the Planck constant. When no complementary ^{12}CO data were available, we took $T_{\text{ex}} = 15$ K, which is the typical kinetic temperature (T_k) of infrared dark clouds^{62,63} and Planck Galactic cold clumps⁶⁴.

The optical depth of ^{13}CO (τ_{13}) of each voxel in the line cube was solved by the radiative transfer equation:

$$\tau_{13} = -\ln \left\{ 1 - \frac{T_{13}}{f_{\text{bm}}[J(T_{\text{ex}}, \nu) - J(T_{\text{bg}}, \nu)]} \right\}, \quad (4)$$

where T_{13} is the main beam temperature of the ^{13}CO line. Therefore, $N_{13\text{CO}}$ was found by integrating τ_{13} along the spectral axis, that is the velocity (ν)⁶⁵:

$$N_{13\text{CO}} = \frac{3k}{8\pi^3 B \mu^2} \exp \left[\frac{h B J_l (J_l + 1)}{k T_{\text{ex}}} \right] \times \frac{T_{\text{ex}} + h B / 3k}{1 - \exp(-h \nu / k T_{\text{ex}})} \times \frac{\int \tau_{13} d\nu}{(J_l + 1)}, \quad (5)$$

where B (~ 55.1 GHz) is the rotational constant, μ (~ 0.112 D) is the dipole moment and J_l is the lower energy level of the ^{13}CO transition (for $^{13}\text{CO } J = 1 \rightarrow 0$, $J_l=0$; for $^{13}\text{CO } J = 2 \rightarrow 1$, $J_l=1$).

We converted $N_{13\text{CO}}$ to N_{H_2} through the abundance ratios of $N_{12\text{CO}}/N_{13\text{CO}}$ (hereafter $^{12}\text{CO}/^{13}\text{CO}$) and $N_{\text{H}_2}/N_{12\text{CO}}$ (hereafter $\text{H}_2/^{12}\text{CO}$) for the Galactic molecular clouds:

$$N_{\text{H}_2} = N_{13\text{CO}} \times ^{12}\text{CO}/^{13}\text{CO} \times \text{H}_2/^{12}\text{CO}. \quad (6)$$

The underlying assumptions are as follows: (1) $^{12}\text{CO}/^{13}\text{CO}$ is represented by the ^{12}C -to- ^{13}C isotopic ratio ($^{12}\text{C}/^{13}\text{C} = 5.87R_{\text{gc}} + 13.25$)³⁵ and (2) $\text{H}_2/^{12}\text{CO}$ is inversely proportional to the gas-phase oxygen abundance ($\text{O}/\text{H} \propto 10^{-0.044(R_{\text{gc}} - R_{\text{gc},\odot})}$)³¹. The $\text{H}_2/^{12}\text{CO}$ value at $R_{\text{gc}} = R_{\text{gc},\odot}$ is 6.0×10^3 , measured by absorption lines in nearby clouds against background stars⁶⁶.

We assumed $\text{H}_2/^{13}\text{CO} = 3 \times 10^6$ (ref. 9,67) for molecular clouds in the LMC. We adopted $\text{H}_2/^{13}\text{CO} = 7.5 \times 10^6$ for the SMC and NGC 6822, which was scaled from the LMC value through their metallicity ratio.

Physical properties of molecular clouds

In this work, the equivalent radius (R_{cloud}), the velocity dispersion (σ_v) and the molecular gas mass (M_{mol}) of molecular clouds were all measured within the half-peak isophote of N_{H_2} . This enabled a consistent comparison among observations with different angular resolutions and sensitivities ('Possible bias in measuring cloud properties'). The measured physical quantities for the Galactic molecular clouds are presented in Supplementary Tables 2 and 3.

• R_{cloud} : The equivalent angular radius (r_{cloud}) of a cloud was calculated by deconvolving the telescope beam from the observed angular area (A ; within the half-peak isophote of N_{H_2}):

$$r_{\text{cloud}} = \sqrt{\frac{A}{\pi} - \frac{\theta_{\text{beam}}^2}{4}}. \quad (7)$$

Theoretically, the fractional uncertainty of r_{cloud} is inversely proportional to the S/N of the peak intensity⁶⁸. Most clouds studied in this work have a peak S/N much larger than 10. Therefore, we adopted a conservative uncertainty of 10% for r_{cloud} ('Possible bias in measuring cloud properties') to include any unforeseen errors. The cloud physical radius is then given by $R_{\text{cloud}} = r_{\text{cloud}} d$.

- σ_v : The intensity-weighted velocity dispersion (σ_v) is given by

$$\sigma_v = \sqrt{\sigma_{v,\text{obs}}^2 - \sigma_{v,\text{ins}}^2}, \quad (8)$$

where $\sigma_{v,\text{obs}} = \sqrt{\sum T_i (v_i - \bar{v})^2 / \sum T_i}$ is the observed velocity dispersion and $\sigma_{v,\text{ins}} = \Delta V_{\text{ins}} / 2\sqrt{2\ln(2)}$ is the velocity dispersion led by the instrumental spectral broadening. $\bar{v} = \sum T_i v_i / \sum T_i$ is the intensity-weighted mean velocity. ΔV_{ins} is approximately the channel width. We also applied an uncertainty of 10% for σ_v .

- M_{mol} : The M_{mol} of a molecular cloud at a distance of d is

$$M_{\text{mol}} = \mu m_{\text{H}_2} d^2 \int_A N_{\text{H}_2} \delta x \delta y, \quad (9)$$

where $m_{\text{H}_2} \approx 3.347115 \times 10^{-24}$ g is the mass of an H_2 molecule, δx and δy are the pixel angular sizes and $\mu \approx 1.36$ is the mean molecular weight considering the mass of helium²⁹. We adopted an uncertainty of 20% for M_{mol} , which is a conservative estimate for the flux calibration error for millimetre-wave observations. Systematic errors are not involved in error propagation.

The mean mass surface density (Σ_{mol}) is

$$\Sigma_{\text{mol}} = \frac{M_{\text{mol}}}{\pi R_{\text{cloud}}^2}. \quad (10)$$

For molecular clouds in DDO 70, Σ_{mol} is related to the cloud-boundary surface density ($\Sigma_{\text{limit}} = 756 \pm 468 M_{\odot} \text{pc}^{-2}$, projection on the two-dimensional sky)⁴¹ by $\Sigma_{\text{mol}} = \frac{2}{-k+3} \Sigma_{\text{limit}}$, for a radial density profile $\rho \propto r^{-k}$. We adopt $k = 1.8$ for typical star forming clumps in the Milky Way⁶⁹.

The virial parameter

The virial parameter (α_{vir}) is defined as¹³:

$$\alpha_{\text{vir}} = \frac{5\sigma_v^2 R_{\text{cloud}}}{GM_{\text{mol}}} = a \frac{2E_k}{|E_g|}, \quad (11)$$

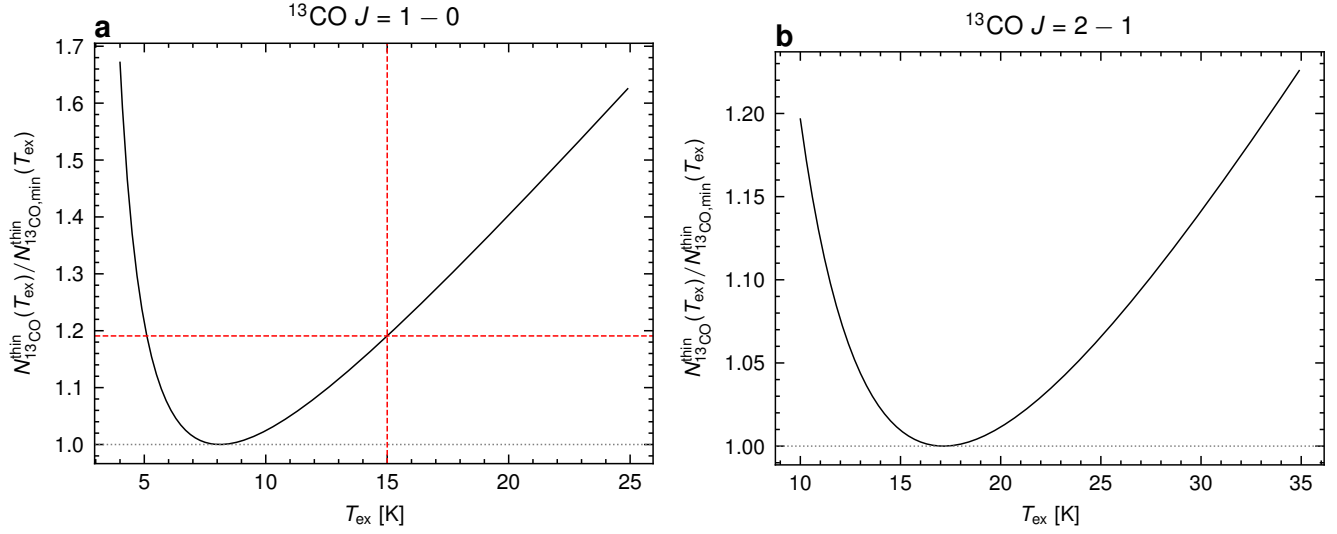
where G is the gravitational constant. For a uniform-spherical cloud ($a = 1$)¹³, if the contributions of both the external pressure and the magnetic field are negligible, virial equilibrium ($2E_k + E_g = 0$) and energy equipartition ($E_k + E_g = 0$) lead to $\alpha_{\text{vir}} = 1$ and $\alpha_{\text{vir}} = 2$, respectively. Even though virial equilibrium and energy equipartition are conceptually different¹², a factor of two in α_{vir} is hard to measure due to the systematic uncertainties. Consequently, we could not distinguish them in this work. Molecular clouds with $\alpha_{\text{vir}} > 1$ and $\alpha_{\text{vir}} < 1$ are defined as supervirial and subvirial, respectively.

Systematic errors in M_{mol} and α_{vir}

The uncertainties in M_{mol} and α_{vir} come from the uncertainties in the cloud distance (d), the excitation conditions of ^{13}CO and the abundance ratios. Among the parameters used to calculate α_{vir} (Eq. 11), both R_{cloud} and M_{mol} depend on the cloud distance. R_{cloud} scales with d . M_{mol} scales with both d^2 and the $\text{H}_2/^{13}\text{CO}$ abundance ratio. The $\text{H}_2/^{13}\text{CO}$ abundance ratio was estimated through the Galactic $^{12}\text{C}/^{13}\text{C}$ gradient and the O/H gradient, and is, therefore, a function of R_{gc} . Therefore, $\alpha_{\text{vir}} \propto d^{-1} (\text{H}_2/^{13}\text{CO})^{-1}$.

The distances of the Galactic outer-disk molecular clouds are well constrained with a fractional uncertainty of $\lesssim 20\%$. For clouds at $R_{\text{gc}} > 15$ kpc, the distance uncertainty contributes $\lesssim 40\%$ of the uncertainty in M_{mol} and $\lesssim 20\%$ of the uncertainty in α_{vir} .

In the following, we assess the systematic errors arising from uncertainties in ^{13}CO excitation conditions and abundance ratios.

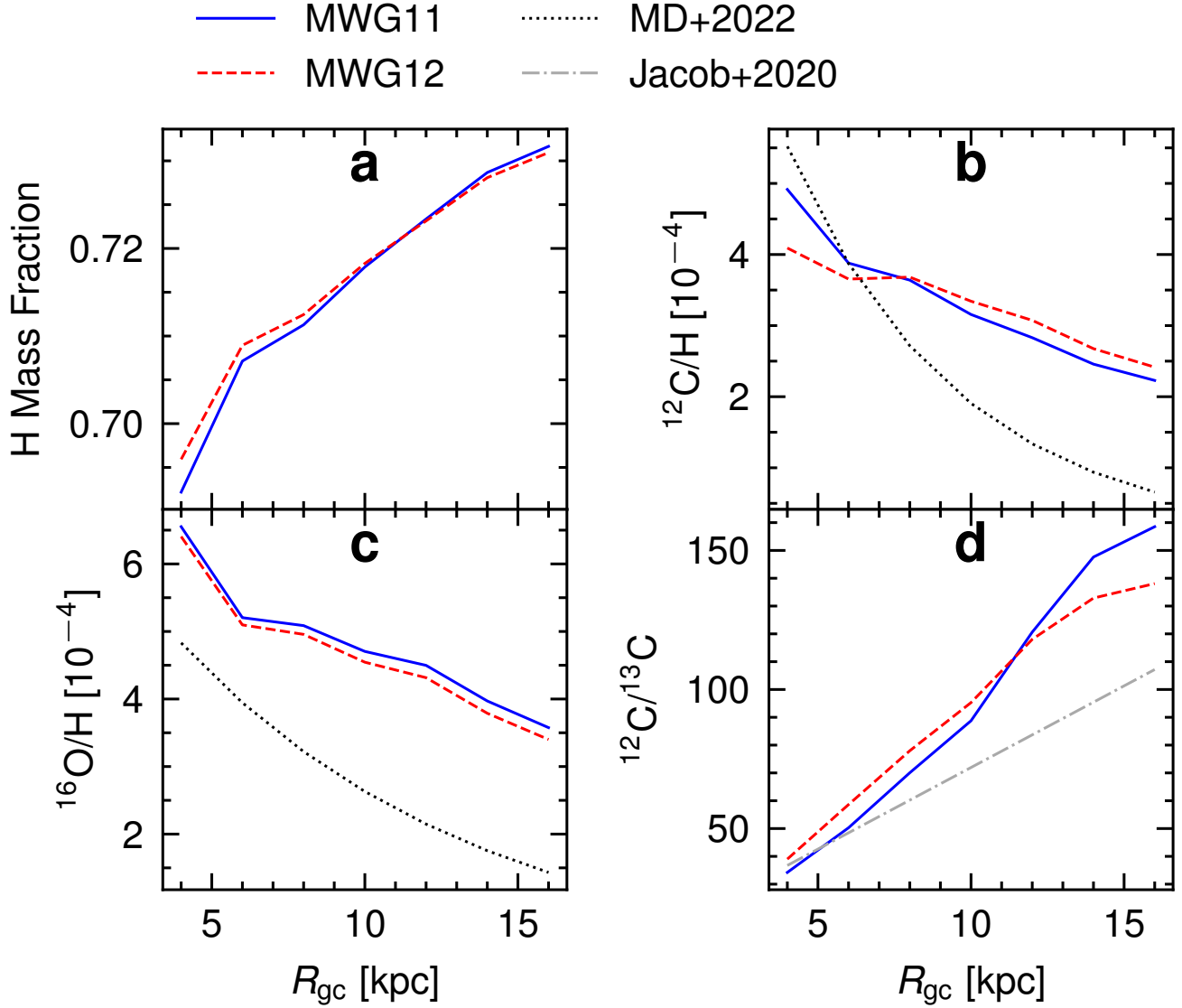


Supplementary Fig. 1: Effect of T_{ex} on $N_{13\text{CO}}$ estimate. We assume that the ^{13}CO lines are in local thermodynamic equilibrium and optically thin. The curves are scaled with respect to their minimum values. **a**, For $^{13}\text{CO } J = 1 - 0$. **b**, For $^{13}\text{CO } J = 2 - 1$.

- The excitation of ^{13}CO . Depending on the specific excitation conditions³, assuming local thermodynamic equilibrium can deviate $N_{13\text{CO}}$ from its intrinsic value. For the typical mean volume density of H_2 (n_{H_2}) of the molecular clouds studied in this work ($\sim 10^3 - 10^4 \text{ cm}^{-3}$), the deviation from the theoretical mass was $\lesssim 40\%$. The assumption of $T_{\text{ex}} = 15 \text{ K}$ may overestimate $N_{13\text{CO}}$ by $\lesssim 20\%$ for the $J = 1 \rightarrow 0$ transition (Supplementary Fig. 1a). The overestimation is negligible for the $J = 2 \rightarrow 1$ transition (Supplementary Fig. 1b). Therefore, the overall overestimation due to the assumptions on ^{13}CO excitation is within 60%.
- The abundance ratios. Not only are the $^{12}\text{C}/^{13}\text{C}$ ratios still poorly measured at $R_{\text{gc}} > 12 \text{ kpc}$ (ref. 35, 70–72) but the Galactic gas-phase O/H versus R_{gc} gradient is also still less constrained at $R_{\text{gc}} > 18 \text{ kpc}$ (ref. 31). Depending on the depth into molecular clouds, the molecular ($^{12}\text{CO}/^{13}\text{CO}$) abundance ratio can be lower than the isotopic ($^{12}\text{C}/^{13}\text{C}$) abundance ratio due to isotopic-selective chemical reactions⁷³. This may have led to an overestimation of $N_{12\text{CO}}$ as inferred from $N_{13\text{CO}}$ by up to 50–60% (ref. 73). The $\text{H}_2/^{12}\text{CO}$ ratios measured in the solar neighbourhood ($R_{\text{gc},\odot}$) also vary by a factor of two among different studies^{66,74,75}. Despite these uncertainties, the dependencies of $^{12}\text{CO}/^{13}\text{CO}$ and $\text{H}_2/^{12}\text{CO}$ on R_{gc} (or Z) are natural expectations of Galactic chemical evolution models (Supplementary Fig. 2)⁷⁶ and astrochemistry⁷⁷. Supplementary Fig. 3 shows a test under an extreme condition, where M_{mol} is calculated with a constant $\text{H}_2/^{13}\text{CO}$ abundance ratio (to simulate what would happen if we were to neglect any abundance gradients). In this case, the α_{vir} trends become flatter. Given both the observational and theoretical evidence for the existence of gradients in both $^{12}\text{C}/^{13}\text{C}$ and O/H with R_{gc} , the α_{vir} trends can be considered as solid, albeit the uncertainties in the gradient slopes.

Possible bias in measuring cloud properties

Limited angular resolution and observational sensitivity may also have biased the measurement of R_{cloud} and M_{cloud} . To examine to what extent these may have influenced our results, we generated a set of mock clouds to mimic real observations. First, we generated two-dimensional Gaussian models as the intrinsic

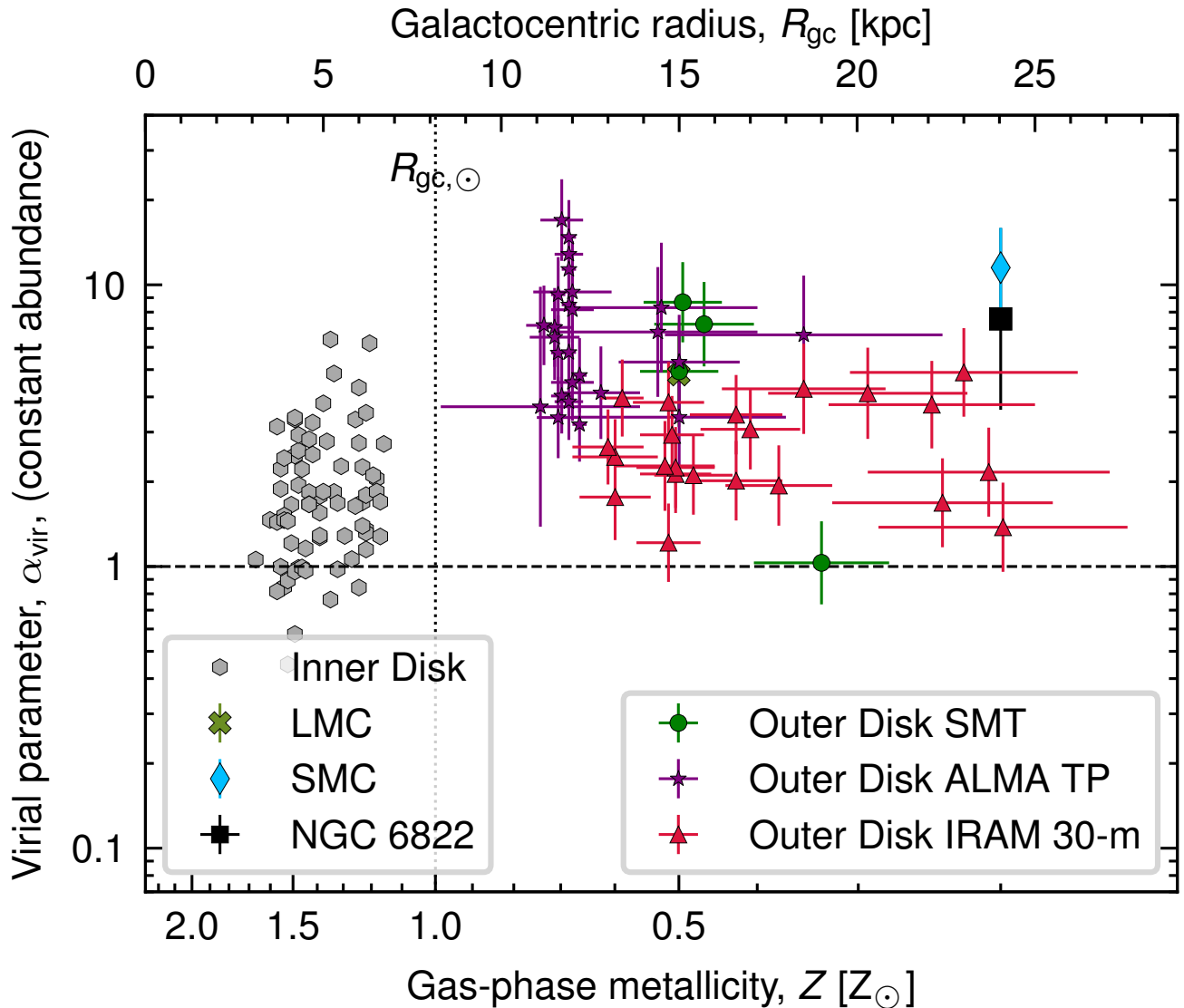


Supplementary Fig. 2: Galactic radial gradients of elemental abundances. In each panel, the blue solid and the red dashed lines show the R_{gc} -gradients predicted by the Galactic Chemical Evolution models⁷⁶. The black dotted lines show the C/H - R_{gc} gradient in **b** and the O/H - R_{gc} gradient in **c** from observations³¹. The grey dash-dotted line in **d** shows the observed $^{12}\text{C}/^{13}\text{C}$ - R_{gc} gradient³⁵.

cloud emissions. We then convolved the Gaussian models with the telescope beam and added Gaussian noise to the convolved models.

The peak values of the Gaussian models were scaled such that the final convolved maps have a peak $S/N = 10$, which is approximately the worst S/N of our sample of Galactic clouds. The major axes of the Gaussian models were set from $4''$ to $100''$ (with a spacing of $0.5''$) and the minor-to-major axis ratios (aspect ratios) were set from 0.2 to 1.0 (with a spacing of 0.2). We used a telescope beam of $23.5''$ and a pixel size of $4''$, the same as for our IRAM 30 m telescope observations. Similarly, we measured the cloud equivalent radii and fluxes within the half-peak isophote of the convolved models.

Supplementary Fig. 4a shows the ratio between the measured radius (r_M) and its true value (r_T) as

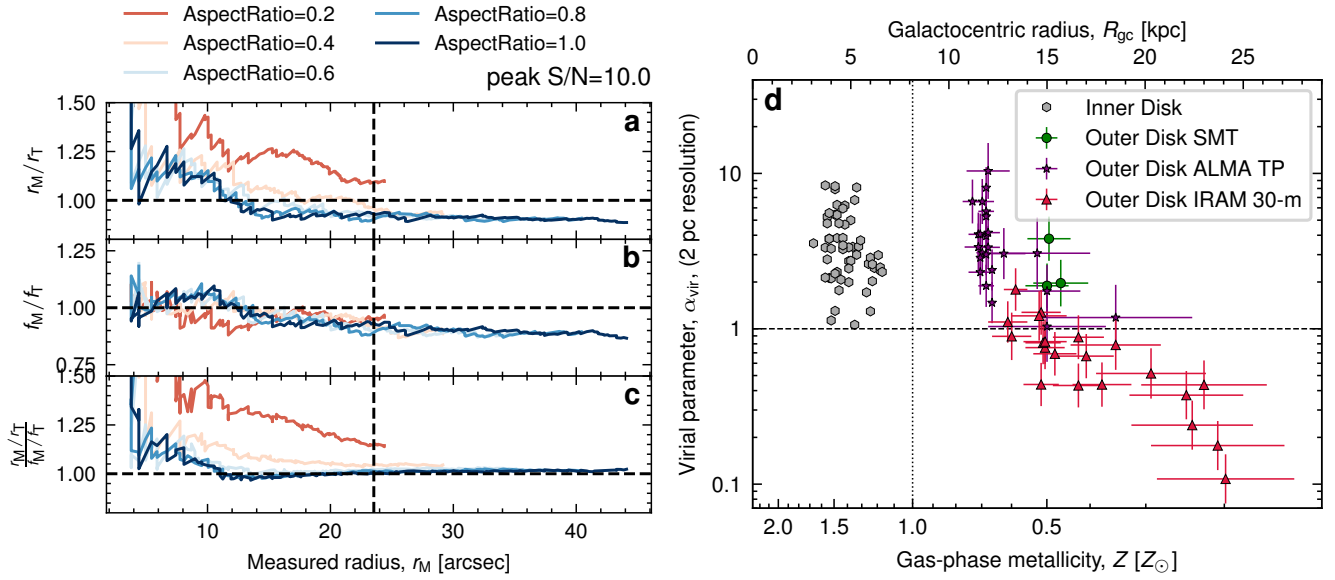


Supplementary Fig. 3: Examining the α_{vir} trends under an extreme assumption. Instead of considering an $\text{H}_2/^{13}\text{CO}$ ratio that varies with R_{gc} (or Z), we convert $N_{^{13}\text{CO}}$ to N_{H_2} using a constant $\text{H}_2/^{13}\text{CO}$ value (set by its value at $R_{\text{gc},\odot}$). Molecular clouds in DDO 70 are not shown in this plot because their cloud masses are measured following a different approach⁴¹. Data are presented as measured values with $1\text{-}\sigma$ uncertainties.

a function of r_{M} . For clouds with an aspect ratio ≥ 0.4 (roundish clouds) and $r_{\text{M}} \gtrsim 10''$ (clouds large enough to be marginally resolved), the difference between r_{M} and r_{T} is within 10%, consistent with the theoretical prediction⁶⁸. In other cases, that is, elongated clouds and small clouds, the cloud radii are overestimated because the minor axes in the convolved models are not well sampled by the image pixel.

Supplementary Fig. 4b shows the ratio between the measured flux (f_{M}) and its true value (f_{T}) as a function of r_{M} . In all cases, the difference between f_{M} and f_{T} is within 10%. Given that the flux ratio is representative of the mass ratio (Eq. 5) for optically thin, low- J ^{13}CO lines, the cloud masses in this work are insensitive to measurement bias.

Consequently, $\frac{r_{\text{M}}/r_{\text{T}}}{f_{\text{M}}/f_{\text{T}}}$ measures the ratio between the measured α_{vir} and its true value. Supplementary



Supplementary Fig. 4: Examining measurement bias led by the spatial resolution. The effect of angular resolution and sensitivity on measuring the cloud angular radius r (panel a), the emission flux f (panel b), and the virial parameter $\propto r/f$ (panel c). The subscripts ‘M’ and ‘T’ refer to the Measured value and the True value, respectively. **d**, Before measuring the cloud physical quantities, all line cubes of the Galactic molecular clouds are spatially smoothed to a uniform physical resolution of 2 pc. Data are presented as measured values with 1- σ uncertainties.

Fig. 4c shows $\frac{r_M/r_T}{f_M/f_T}$ as a function of r_M . The measured α_{vir} was almost identical to its true value unless the cloud was too small to be sampled by the image pixel, where the α_{vir} is overestimated. Given that most of the clouds in this work have peak $S/N > 10$ and $r_M > 10''$, the angular resolution and the sensitivity do not bias the measurement of α_{vir} .

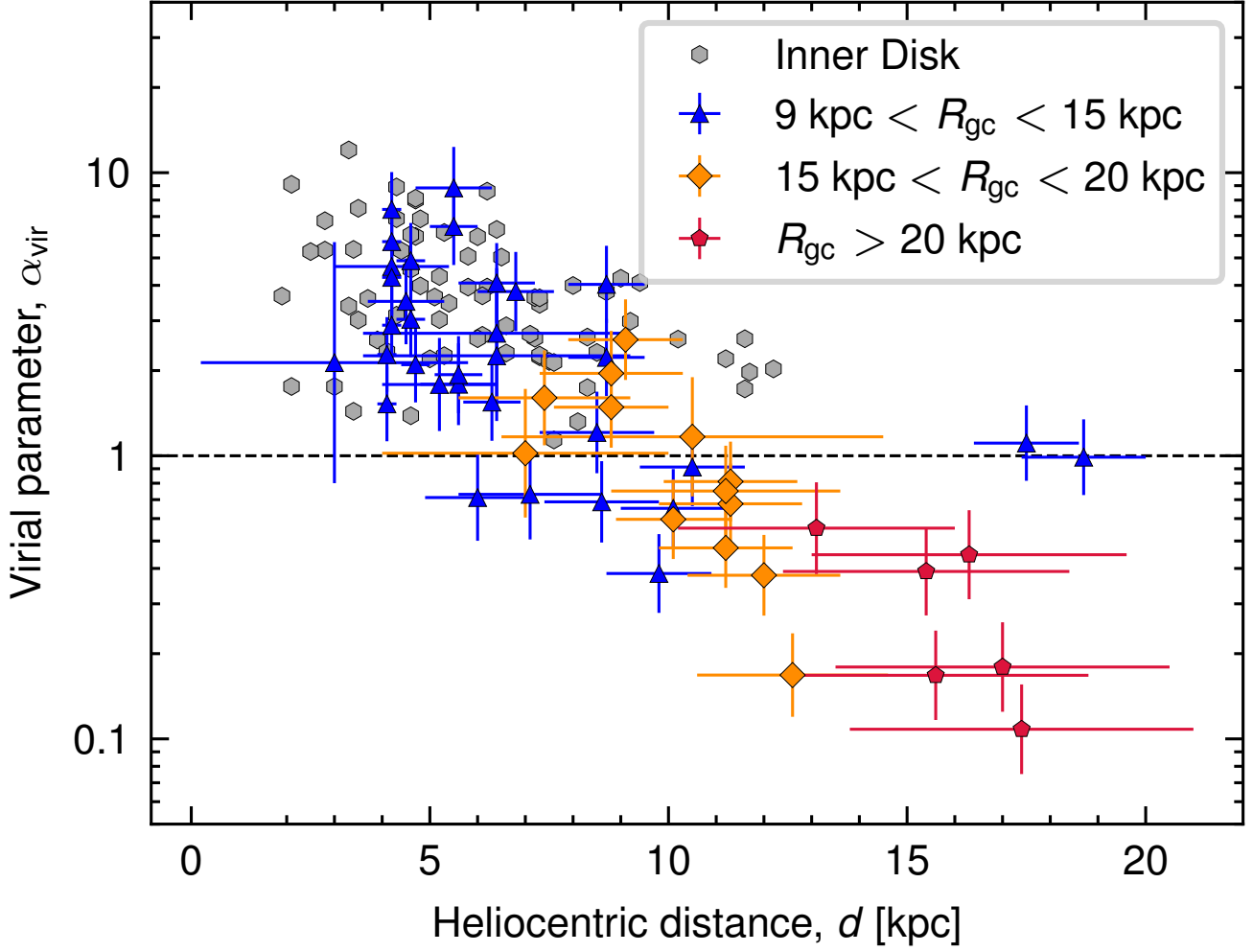
Given the wide range of cloud distances in the Milky Way, a specific telescope beam corresponds to different physical resolutions. We, thus, further tested to see whether this biased our measurements of the cloud α_{vir} . First, we smoothed all line cubes for the Galactic molecular clouds to the same physical resolution of 2 pc, where the smoothing kernels depend on the cloud distances. A few clouds were excluded due to their small (physical) mapping areas. Then, we followed the same procedures to measure the cloud α_{vir} . Supplementary Fig. 4d shows that the α_{vir} trends are not affected by the downgraded physical resolution.

Selection bias

A larger heliocentric distance could bias the sample to brighter (and, thus, more massive) molecular clouds, which tend to have smaller α_{vir} in observations⁷⁸.

We examined whether the decreasing α_{vir} trends were biased by such selection effects by comparing molecular clouds with different R_{gc} but similar heliocentric distances (Supplementary Fig. 5). At the distance range $\sim 15 - 20$ kpc, the sample contains two molecular clouds at $R_{gc} \approx 13$ kpc (G37.350 and G44.8 in the first Galactic quadrant) and five molecular clouds at $R_{gc} > 20$ kpc (SUN15_56, SUN15_57, SUN15_53, SUN15_55, and SUN15_59 in the second Galactic quadrant). The clouds at $R_{gc} > 20$ kpc have at least $\times 5$ smaller α_{vir} than those at $R_{gc} \approx 13$ kpc.

Supplementary Fig. 6a,b show that for each R_{gc} bin, α_{vir} barely varies with M_{mol} or n_{H_2} . At comparable



Supplementary Fig. 5: Examining bias led by the heliocentric distance. Variation of α_{vir} with d . The outer disk clouds are divided into three R_{gc} bins. Data are presented as measured values with $1-\sigma$ uncertainties.

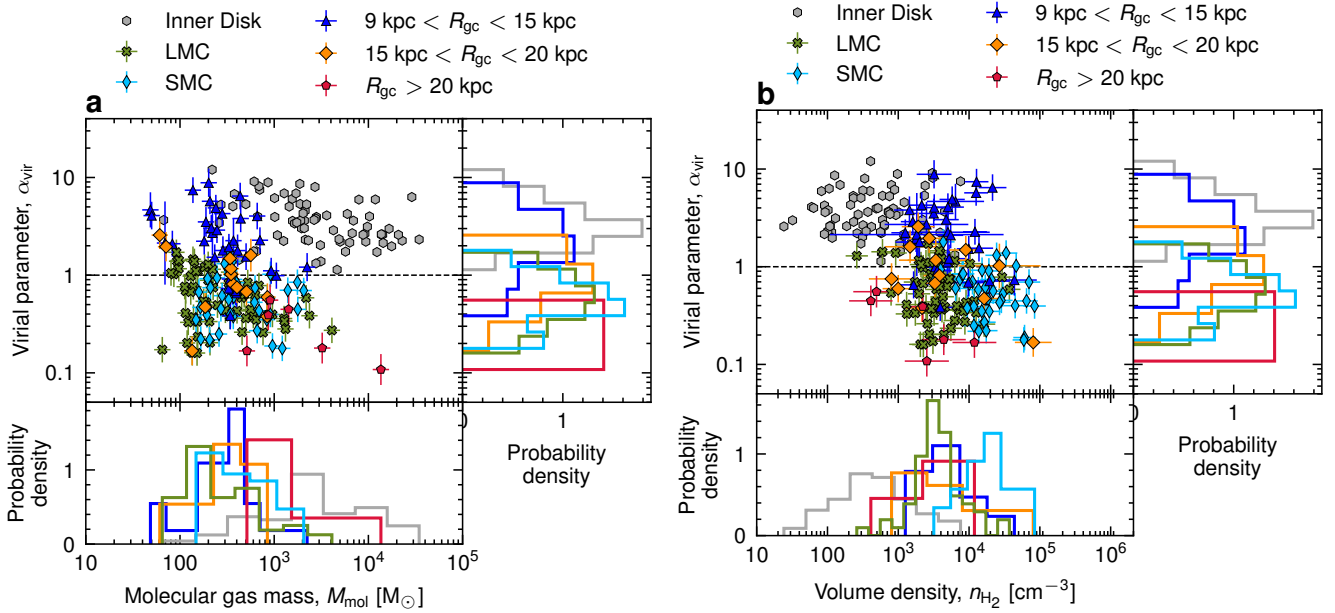
M_{mol} , α_{vir} becomes smaller for larger R_{gc} (reminiscent of predictions by analytic models on Giant Molecular Cloud scales⁷⁹). Therefore, the distance bias to the α_{vir} trends is not important.

The general virial theorem

From the momentum equation, the general Virial Theorem in the presence of external pressure and magnetic fields can be derived^{11,13,43} as:

$$\frac{\dot{I}}{2} = 2(E_k - E_{k,0}) + E_m + E_g, \quad (12)$$

where $E_k = \frac{3}{2}M_{\text{mol}}\sigma_v^2$ is the kinetic energy and $E_g = -a\frac{3GM_{\text{mol}}^2}{5R_{\text{cloud}}}$ is the self-gravitational energy (a is of order unity and accounts for the non-sphericity and the non-uniformity of a molecular cloud). $E_{k,0} = \frac{3P_e V}{2}$ and $E_m = \frac{1}{8\pi} \int (B^2 - B_e^2) dV$ account for the external pressure (P_e) and the magnetic field (B), surrounding and within the cloud volume (V), respectively. B_e is the magnetic field outside the cloud.



Supplementary Fig. 6: Examining bias led by the molecular gas mass and the mean volume density. **a**, The upper left panel shows the variation of α_{vir} with M_{mol} . All molecular clouds in the LMC and the SMC are plotted. The upper right and the lower left panels show the probability density distribution of α_{vir} and M_{mol} for different cloud samples. **b**, Variation of α_{vir} with n_{H_2} . Data are presented as measured values with $1\text{-}\sigma$ uncertainties.

For the general virial equilibrium, the second-derivative of the moment of inertia (\ddot{I}) equals zero unless tidal fields are dominant within a cloud volume, which may be the case for clouds in the Galactic Centre. In Eq. 12, only the volumetric $\frac{1}{8\pi} \int B^2 dV$ term inside E_{m} has the sign that allows it to serve as another support in the dynamic state of the cloud besides E_{k} .

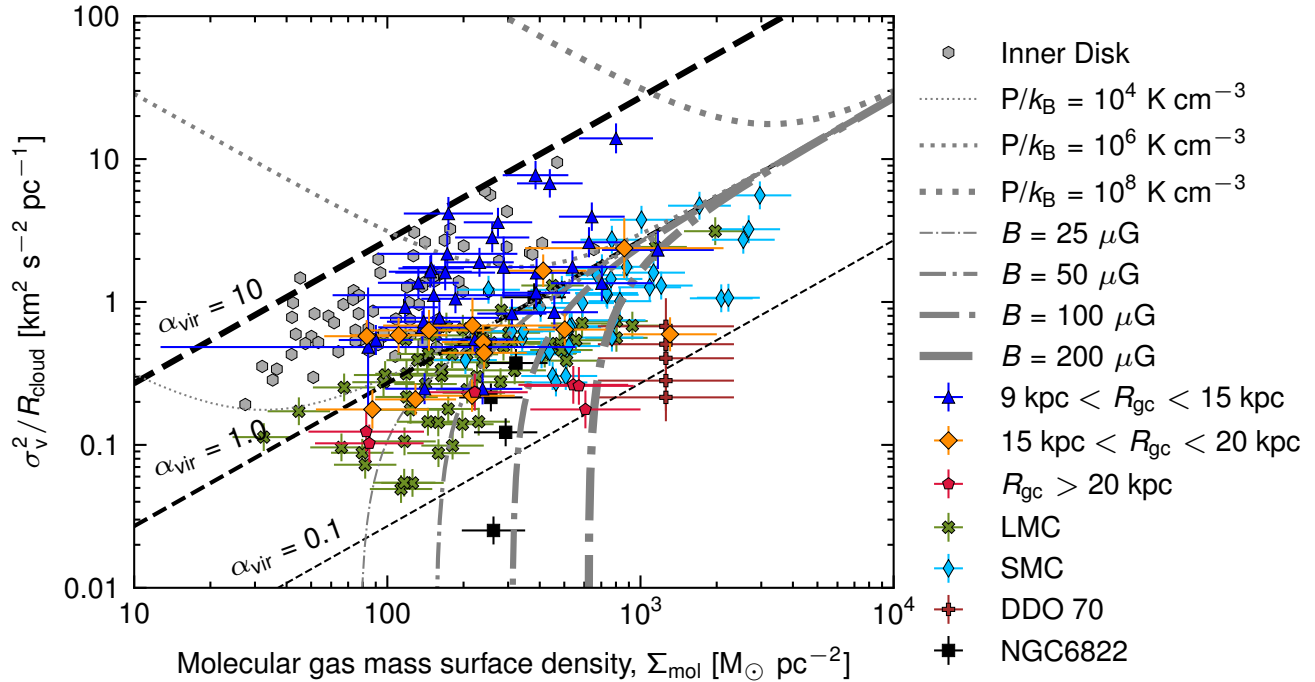
For the supervirial molecular clouds, the support from the B field is often negligible due to the strong turbulence. If these clouds are in general virial-equilibrium, they are most probably bound by P_{e} (lines of constant pressures in Supplementary Fig. 7)^{11,13,48}:

$$\frac{\sigma_{\text{v}}^2}{R_{\text{cloud}}} = \frac{\pi G \Sigma_{\text{mol}}}{5} + \frac{4P_{\text{e}}}{3\Sigma_{\text{mol}}}. \quad (13)$$

Supervirial α_{vir} values are often deduced for molecular clouds in the centres of galaxies and are thought to be responsible for the lower X_{CO} values found for them^{80,81}.

For the subvirial clouds, the B field starts to dominate the support against cloud self-gravity. The supporting force from the B field is indirectly exerted on the neutral molecular gas through ion-neutral collisions. Given the representative volume density ($n_{\text{H}_2} \approx 10^3 - 10^4 \text{ cm}^{-3}$) of the outer-disk clouds and a typical cosmic-ray ionization rate ($\zeta_{\text{H}_2} = 10^{-17} \text{ s}^{-1}$)^{82,83}, the typical ionization fraction ($x_{\text{e}} = n_{\text{e}}/n_{\text{H}}$)⁴⁴ is $\sim 10^{-7}$. This results in a magnetohydrodynamic cutoff wavelength of $\lesssim 0.01 \text{ pc}$ (ref.⁴⁴). Therefore, for the typical scale ($\sim 1 \text{ pc}$) of the outer-disk molecular clouds, the magnetic fields are well coupled with neutral particles. Neglecting the minor contribution from P_{e} in the outer Galaxy, we can derive (lines with constant B fields in Supplementary Fig. 7):

$$\frac{\sigma_{\text{v}}^2}{R_{\text{cloud}}} = \frac{\pi G \Sigma_{\text{mol}}}{5} - \frac{B^2}{18\pi \Sigma_{\text{mol}}}. \quad (14)$$



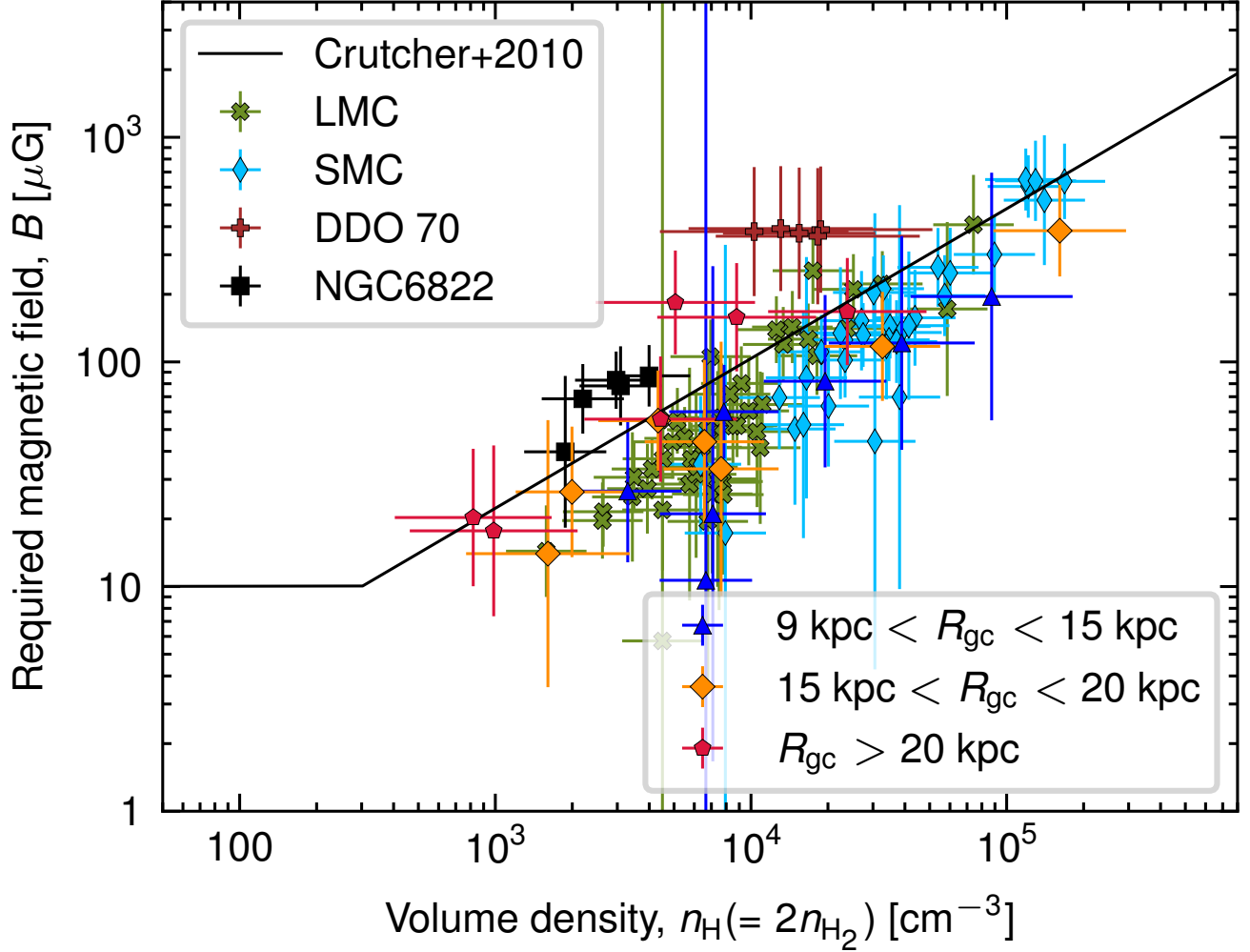
Supplementary Fig. 7: Dynamic analysis based on the general virial theorem. The black dashed lines show $\alpha_{\text{vir}} = 0.1, 1, \text{ and } 10$. Molecular clouds with $\alpha_{\text{vir}} > 1$ and $\alpha_{\text{vir}} < 1$ are super-virial and sub-virial, respectively. Assuming the general virial theorem (see Methods), the super-virial molecular clouds should be bound by external pressure (P_e) while the sub-virial molecular clouds should be supported by magnetic fields (B). The grey dotted lines correspond to $P_e = 10^4, 10^6, \text{ and } 10^8 \text{ k}_B \text{ K cm}^{-3}$. The grey dash-dotted lines correspond to $B = 25, 50, 100, \text{ and } 200 \mu\text{G}$, from thin to thick. Data are presented as measured values with $1\text{-}\sigma$ uncertainties.

Here we neglect the external magnetic field B_e term as it is small ($\sim 10 \mu\text{G}$)⁸⁴ compared to the B field required to support the subvirial clouds ($\sim 100 \mu\text{G}$), as we show below.

Supplementary Fig. 8 compares the B field required to support the subvirial clouds with the expectations from the B versus n_{H} relation ($n_{\text{H}} = 2n_{\text{H}_2}$)^{45,85}. This relation was established in the solar neighbourhood and the inner Galaxy by measuring Zeeman effects. A classical explanation of this relation is that the B -field line is coupled with the molecular gas through ion-neutral coupling⁴⁷ (which is solid at $> 0.01 \text{ pc}$ scales). In denser regions ($n_{\text{H}} > 300 \text{ cm}^{-3}$), the field lines are squeezed by the self-gravity of a cloud, so the B field is enhanced⁴⁵. There are also other explanations⁸⁶.

Supplementary Fig. 8 suggests that a similar B -field strength to those in the inner Galaxy is sufficient for supporting the subvirial clouds in the outer Galaxy. In nearby Milky Way-like spiral galaxies, the energy density of the B field (proportional to B^2) on kiloparsec scales varies only a little from the inner to the outer galactic disk (except for the innermost regions)^{87,88}. If this is also true for the Milky Way, we expect that the B field in molecular clouds will be similar across the Galactic plane, provided that the mechanisms for enhancing the B field with density are similar.

Possible deviations from a uniform-spherical cloud ($a > 1$) would even further consolidate our results. This is because α_{vir} defined by Eq. 11 overestimates $2E_k/|E_g|$ by a factor of a . Given the typical density profiles of Galactic star-forming clouds⁶⁹, $a \sim 1.4 \pm 0.3$. To properly measure a , high-angular-resolution observations are needed⁸⁹.



Supplementary Fig. 8: Variation of the magnetic field strength required to support the sub-virial clouds as a function of the gas volume density. In molecular clouds, the gas volume density is $n_{\text{H}} = 2n_{\text{H}_2}$. The B -field required for supporting the sub-virial molecular clouds is calculated from Eq. 14, which is derived from the general virial theorem. The $B - n_{\text{H}}$ relation benchmarked through observations in the Solar neighborhood and the inner Galaxy⁴⁵ is overlaid as the black solid curve. Data are presented as measured values with $1-\sigma$ uncertainties.

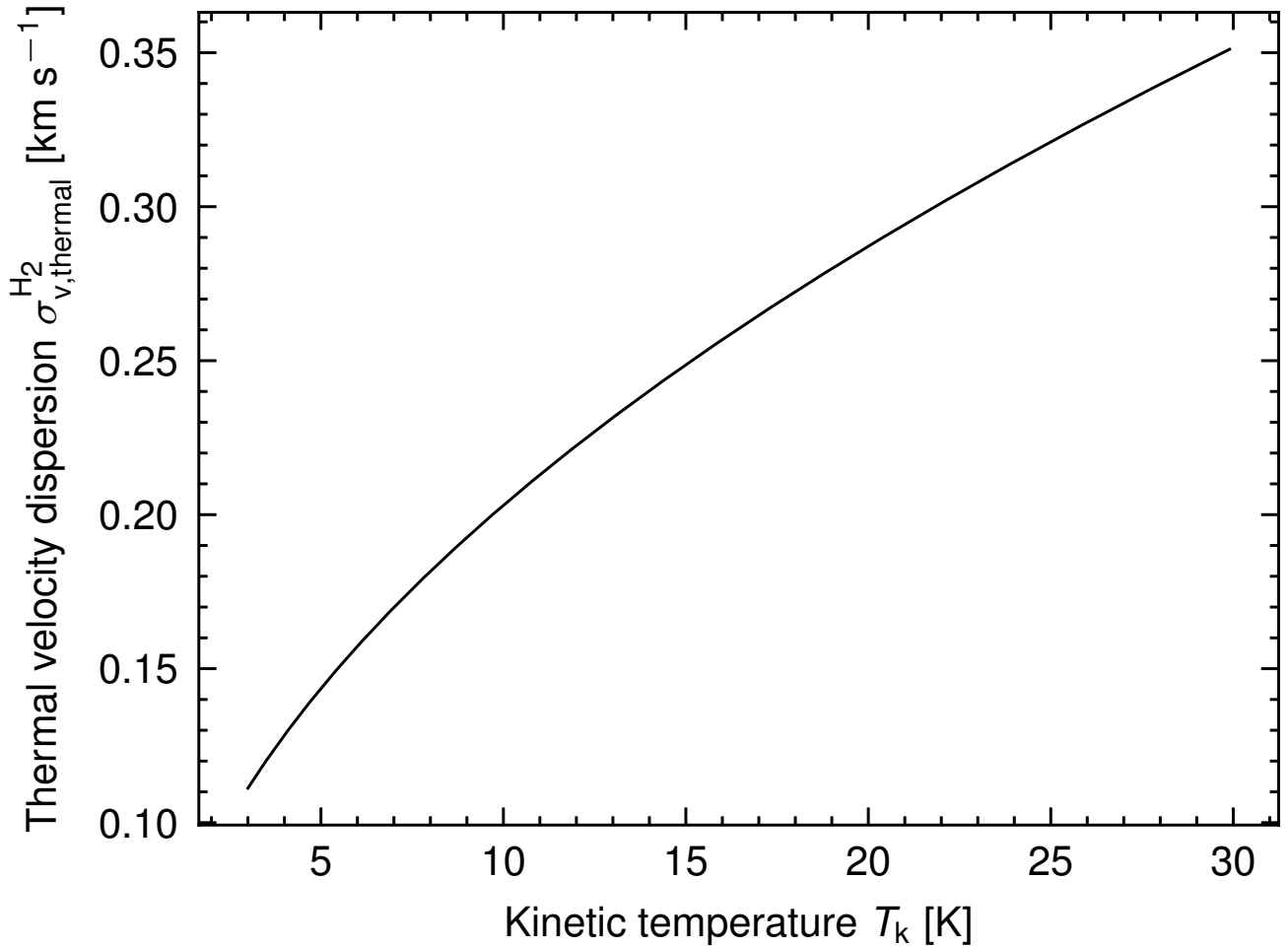
Contribution from cloud rotation and thermal motion in E_{k}

In addition to the random turbulent motion, cloud rotation and thermal motion can also contribute to the σ_{v} of a molecular cloud. To evaluate the effect of cloud rotation, we first fitted the rotational velocity along each LoS with a planar function:

$$v_{\text{rot}}(x, y) = a(x - x_0) + b(y - y_0) + v_0, \quad (15)$$

where (x_0, y_0) is the centre coordinate and v_0 is the LoS velocity at (x_0, y_0) . Then we subtracted the rotational velocity along each LoS in Eq. 8 through

$$\sigma_{\text{v,obs}}^{\text{non-rot}} = \sqrt{\frac{\sum T_i (v_i - \bar{v} - v_{\text{rot}})^2}{\sum T_i}}. \quad (16)$$



Supplementary Fig. 9: Thermal broadening of H₂. Variation of thermal velocity dispersion of H₂ ($\sigma_{v,\text{thermal}}^{\text{H}_2}$) with kinetic temperature (T_k).

The contribution of cloud rotation in E_k is $\lesssim 10\%$.

The thermal broadening of ^{13}CO ($\sigma_{v,\text{thermal}}^{^{13}\text{CO}}$) at $T_k = 15$ K is ~ 0.07 km s^{-1} , which is negligible in σ_v . However, molecular clouds are composed mostly of H₂ molecules, which are lighter than ^{13}CO molecules. Therefore, at the same temperature, the thermal velocity dispersion of H₂ should be larger than that of ^{13}CO . For $T_k = 15$ K, $\sigma_{v,\text{thermal}}^{\text{H}_2} = 0.25$ km s^{-1} (Supplementary Fig. 9). For the outer-disk molecular clouds, the smallest σ_v is ~ 0.30 km s^{-1} . Therefore, for the most extreme cases, including the thermal motion in the total E_k would increase α_{vir} by $\lesssim 70\%$.

Possible mechanisms for B -field-dominated cloud dynamics at low metallicities

Our results reveal that the dynamics of metal-poor clouds may be dominated by the B field. However, the detailed underlying physical mechanisms are still unclear. Here we propose two speculations that may play a role.

First, as was revealed by magnetohydrodynamic simulations⁴⁶, the velocity dispersion of the cold neutral medium decreases towards low metallicity. As molecular clouds should inherit the dynamic properties from their parental ambient atomic gas⁴⁹, they are also expected to have low turbulence levels in low-metallicity conditions. This is in line with Fig. 2b as well as the narrow CO linewidths found in

the LMC and SMC^{5,42}. The cold neutral medium surrounding metal-poor molecular clouds, which has a higher fraction under low-metallicity conditions, may allow turbulence to dissipate significantly enough before entering the molecular clouds. In this case, the B field would take over the role of supporting clouds against self-gravity, resulting in a low α_{vir} observed in metal-poor molecular clouds.

Second, the far-ultraviolet photons can penetrate deeper into molecular clouds in low-metallicity conditions, leading to a higher ionization fraction. This would allow stronger coupling between neutrals and ions regulated by the B field⁴⁷ in such conditions. This could enhance the B-field contribution in supporting these clouds, thus decreasing α_{vir} .

Apart from the above mechanisms, the ^{13}CO molecules could preferentially survive in regions with high column densities, under low-metallicity conditions. This may cause a bias towards the dense cores of molecular clouds, which are often found subvirial with high-volume-density gas tracers^{78,90}. However, the low-metallicity clouds in this work have a typical size of ~ 1 pc, which is larger than dense cores in the solar neighbourhood. This indicates that the B field is already important on cloud scales under low metallicities.

Low turbulence injection and star-formation activities in the Galactic outer disk

In the Milky Way, the turbulence-injection level is expected to decrease towards the outer Galaxy. Turbulence in molecular clouds can be driven by both global Galactic dynamics^{49,79,91} and local stellar feedback^{92,93}. On galactic scales, both shear (Oort constant A) and vorticity (Oort constant B) induced by Galactic differential rotation decline with R_{gc} (Supplementary Fig. 10), leading to less kinetic energy (proportional to $2A^2 + 5B^2$) injected by cloud-cloud collisions⁹⁴. On the other hand, the surface density of the Galactic star formation rate (Σ_{SFR}) decreases with R_{gc} (ref. 95,96), so the effect of stellar feedback effect should also be weak in the outer Galaxy.

To examine the star-formation activities in the outer-disk clouds studied in this work, we compared mid-infrared (3.4, 4.6, 12 and 22 μm wavelength) continuum images from the Wide-field Infrared Survey Explorer archive and radio continuum images from the Very Large Array Sky Survey (3 GHz S-band) and the National Radio Astronomy Observatory's Very Large Array Sky Survey (1.4 GHz L-band). Four clouds did not have archival radio data.

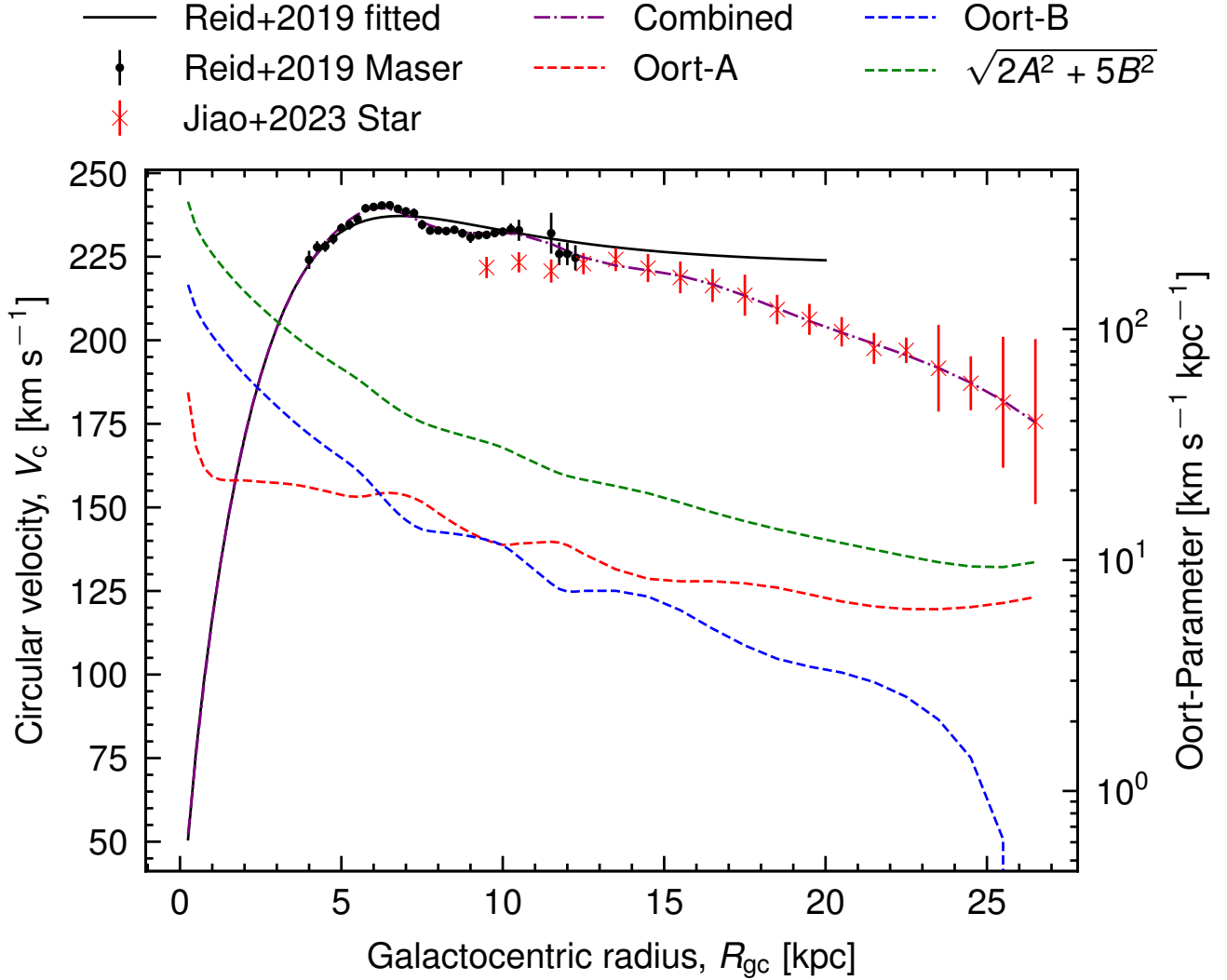
Although most of the outer-disk molecular clouds show obvious 22 μm emissions, only a few of them show obvious 3 and 1.4 GHz continuum emission ('Data Availability'). Therefore, the outer-disk molecular clouds studied in this work are mostly star-forming clumps⁹⁷ without strong massive stellar feedback (otherwise, the 3 and 1.4 GHz continua would show strong free-free emission from H II regions and the velocity dispersion would be increased by the massive stellar feedback). Because the feedback from low-mass stars does not influence the overall cloud dynamics^{98,99}, the α_{vir} trends should also apply to non-star-forming clouds in general.

The subvirial outer-disk clouds at $R_{\text{gc}} > 15$ kpc used in this work are from ref. 52. A sensitive survey of H_2O , CH_3OH and OH masers was performed towards these clouds¹⁰⁰, but no detection was found. This is in line with the evidence that the outer-disk molecular clouds lack massive star formation and, therefore, the stellar feedback is weak.

Caveats of studying α_{vir} using low- J ^{12}CO lines

Low- J ^{12}CO lines, with the standard X_{CO} conversion factor, have been widely adopted to trace molecular gas conditions among H_2 clouds in both the Milky Way and external galaxies¹⁸. However, this method is strictly limited in large-scale studies (50 pc to kiloparsecs)¹⁸. For resolved studies of individual molecular clouds, radiative trapping becomes dominant in regulating the ^{12}CO emission.

First, the optical depths are not uniformly distributed in the ^{12}CO $J = 1 \rightarrow 0$ emission (in both the

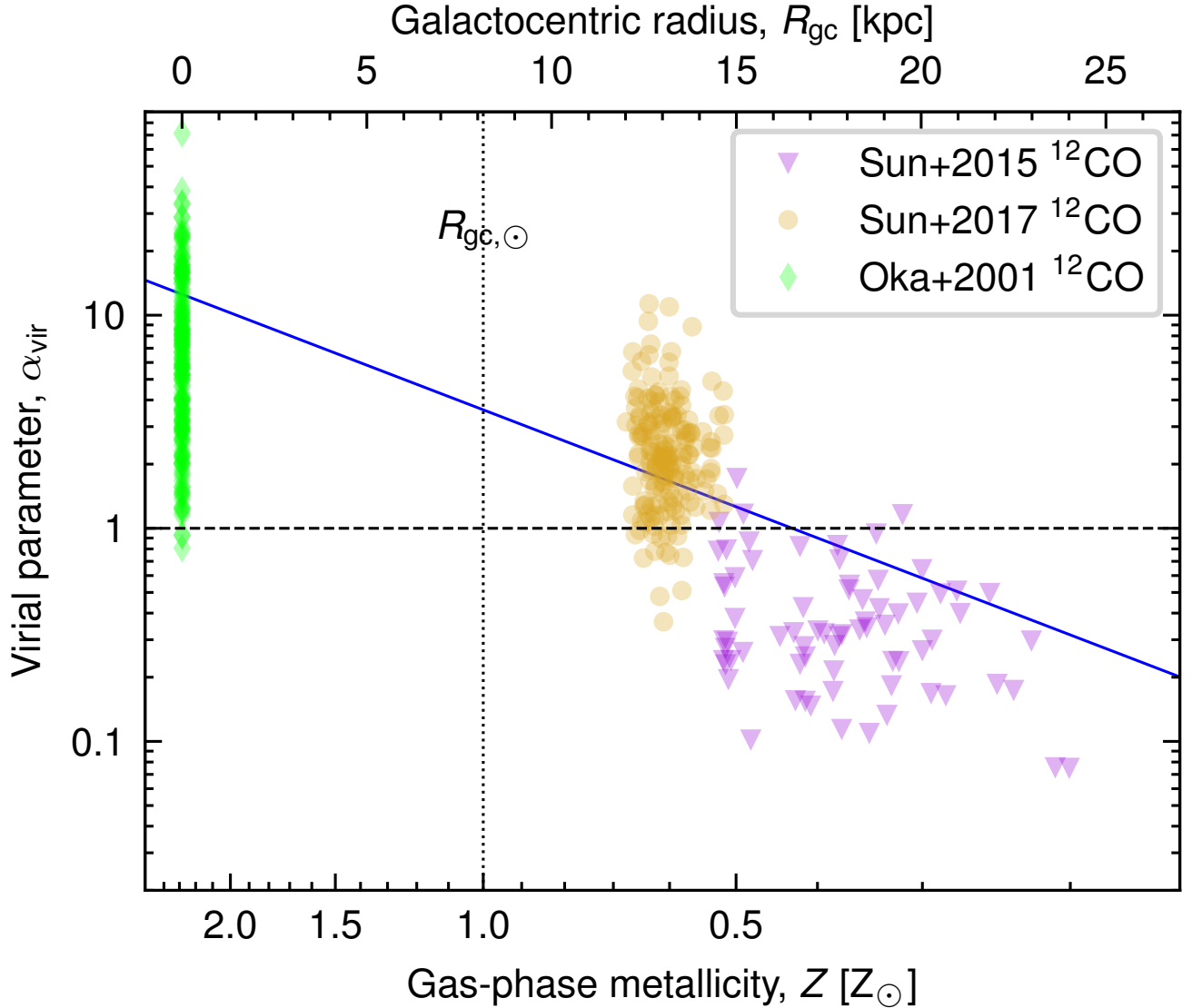


Supplementary Fig. 10: The Galactic rotation curve and the Oort parameters. The Galactic radial profile of the Circular Velocity (V_c) derived by different methods are shown as black solid line/dots³⁶ and red errorbars¹⁰⁶). The combined rotation curve (purple dash-dotted line) is adopted to calculate the Oort-A (red dashed line) and Oort-B (blue dashed line) parameters⁹⁴, which measure the strength of shear and vorticity due to the Galactic rotation curve, respectively. The green dashed line shows the square root of the kinetic energy ($\propto 2A^2 + 5B^2$) led by the Galactic differential rotation⁹⁴. Data are presented as measured values with $1\text{-}\sigma$ uncertainties.

spatial and velocity domains). A simple X_{CO} factor cannot properly trace the real distributions of mass and velocity of H_2 gas.

Second, the effective critical density of the $^{12}\text{CO } J = 1 \rightarrow 0$ line is low. At a kinetic temperature of 20 K and under the optically thin limit¹⁰¹, the critical density n_{crit} of $^{12}\text{CO } J = 1 \rightarrow 0$ is $\sim 3.5 \times 10^2 \text{cm}^{-3}$ (‘Code Availability’). This value is $\times 10$ lower than that often seen in the literature¹⁰², which neglects that collisions do not follow any selection rules¹⁰¹.

However, the $^{12}\text{CO } J = 1 \rightarrow 0$ line shows a high optical depth (with a mean value $\tau > 10$, by multiplying the $^{12}\text{C}/^{13}\text{C}$ ratio with $\tau_{^{13}\text{CO}}$)²⁴ in Galactic giant molecular clouds, indicating strong local



Supplementary Fig. 11: Variation of α_{vir} with Z and R_{gc} . The α_{vir} are measured using ^{12}CO emission from^{52,54,104}. The blue line shows a linear fitting of the $\alpha_{\text{vir}}-Z$ trend using the ^{13}CO data in the Milky Way (see Methods). Data are presented as measured values with $1-\sigma$ uncertainties.

radiative trapping¹⁰³. This radiative trapping would lower the effective critical density $n_{\text{crit}}^{\text{eff}}$ by another factor of τ (>10): $n_{\text{crit}}^{\text{eff}} \approx n_{\text{crit}}(1 - e^{-\tau})/\tau$, where $(1 - e^{-\tau})/\tau \approx 1/\tau$ represents the escape probability of the transition. This means that H_2 gas with a low density of a few $\times 10 \text{ cm}^{-3}$ could remarkably contribute to the $^{12}\text{CO } J = 1 \rightarrow 0$ emission in both line flux and linewidth.

As a sanity check, we also collected ^{12}CO measurements from the literature^{52,54,104}. We corrected M_{mol} by implementing the metallicity-dependent X_{CO} . We simply adopted $X_{\text{CO}} \propto Z^{-1.0}$ as the dependency relation¹⁸. Supplementary Fig. 11 shows that the α_{vir} measured using ^{12}CO emission follows a similar trend ^{13}CO : $\log(\alpha_{\text{vir}}) = (1.5 \pm 0.1) \times \log(Z/Z_{\odot}) + (0.56 \pm 0.03)$. This correlation was fitted using ordinary least squares for the ^{13}CO measurements of the Galactic molecular clouds (Fig. 3). The slope of the α_{vir} versus Z trend is sensitive to the adopted $\text{H}_2/^{13}\text{CO}$ abundance ratio, which may be better constrained by future observations.

Data Availability

The following data and figures are available via figshare at <https://doi.org/10.6084/m9.figshare.27282924> (ref.105): (1) reduced data cubes of the new observations presented in this work (subfolder GMPMC_line_fitscubes), (2) ^{13}CO spectra and N_{H_2} maps (subfolder Supp_Figures/NH2_13CO_spectrum), (3) infrared and radio images (subfolder Supp_Figures/IR_Radio_outer_disk_clouds) and (4) distance PDFs of the Galactic molecular clouds (subfolder Supp_Figures/Distance_PDFs). This work is based on observations carried out under Projects 031-17 and 102-22 with the IRAM 30 m telescope, Projects ADS/JAO.ALMA#2013.1.00652.S, ADS/JAO.ALMA#2015.1.00581.S, ADS/JAO.ALMA#2019.1.01641.S and ADS/JAO.ALMA#2021.2.00175.S with ALMA, and Project Lin_L_22B_1 with SMT. Source data are provided with this paper.

Code Availability

Code for calculating the critical densities can be obtained from GitHub (https://github.com/ZhiyuZhang/critical_densities).

Acknowledgements

This work is supported by the National Key Research & Development (R&D) Programme of China (Grant No. 2023YFA1608204). Z.-Y.Z., L. Lin, Yichen Sun and G.L. acknowledge the support of the National Natural Science Foundation of China (NSFC; Grant Nos. 12173016 and 12041305), science research grants from the China Manned Space Project (Grant Nos. CMS-CSST-2021-A08 and CMS-CSST-2021-A07) and the Programme for Innovative Talents, Entrepreneur in Jiangsu. This work also benefited from the International Space Science Institute (ISSI/ISSI-BJ) in Bern and Beijing, thanks to funding for the team ‘Chemical abundances in the ISM: the litmus test of stellar IMF variations in galaxies across cosmic time’ (PIs D.R. and Z.-Y.Z.). J. Wang gives thanks for the support of the NSFC (Grant No. 12173067) and the Guangxi Talent Programme (Highland of Innovation Talents). Y.G. is supported by the Strategic Priority Research Programme of the Chinese Academy of Sciences (Grant No. XDB0800301). Yan Sun is supported by the Youth Innovation Promotion Association, CAS (Grant No. 2022085), and the Light of West China Programme (Grant No. xbzg-zdsys-202212). T.G.B. acknowledges support from the Leading Innovation and Entrepreneurship Team of Zhejiang Province of China (Grant No. 2023R01008). D.R. thanks the Italian National Institute for Astrophysics for funding the project ‘An in-depth theoretical study of CNO element evolution in galaxies’ through Finanziamento della Ricerca Fondamentale, Theory Grant Fu. Ob. 1.05.12.06.08. D.L. is a New Cornerstone investigator. H.B.L. is supported by the National Science and Technology Council of Taiwan (Grant Nos. 111-2112-M-110-022-MY3 and 113-2112-M-110-022-MY3). K.Q. acknowledges support from the NSFC (Grant Nos. 12425304 and U1731237) and the National Key R&D Programme of China (Grant Nos. 2023YFA1608204 and 2022YFA1603100). C.-W.T. is supported by the NSFC (Grant No. 11988101). J. Wu gives thanks for support from the NSFC (Grant No. 12041302) and the Tianchi Talent Programme of Xinjiang Uygur Autonomous Region. S.F. acknowledges support from the NSFC (Grant No. 12373023), a starting grant at Xiamen University and the presidential excellence fund at Xiamen University (Grant No. 20720220024). This work is based on observations carried out under Projects 031-17 and 102-22 with the IRAM 30 m telescope, Projects ADS/JAO.ALMA#2013.1.00652.S, ADS/JAO.ALMA#2015.1.00581.S, ADS/JAO.ALMA#2019.1.01641.S and ADS/JAO.ALMA#2021.2.00175.S with ALMA, and Project Lin_L_22B_1 with SMT. IRAM is supported by INSU/ CNRS (France), MPG (Germany) and IGN (Spain). ALMA is a partnership of ESO (representing its member states), NSF (USA) and NINS (Japan),

together with NRC (Canada), MOST and ASIAA (Taiwan) and KASI (Republic of Korea), in cooperation with the Republic of Chile. The Joint ALMA Observatory is operated by ESO, AUI/NRAO and NAOJ. The Heinrich Hertz SMT is operated by the Arizona Radio Observatory, which is part of Steward Observatory at the University of Arizona.

Author Contributions statement

L. Lin led the project, conducted the data reduction and analyses, and drafted proposals and the paper. Z.-Y.Z. initiated and supervised the whole project and improved the paper. J. Wang helped with the data analysis and validating tests. P.P.P. instructed the general virial analysis and outlined the larger theoretical picture. Yong Shi helped extend this work to low-metallicity dwarf galaxies. Y.G. helped improve the paper and was involved in discussions. Yan Sun provided the initial catalogue and helped with calculating the cloud distances. Yichen Sun, T.G.B. and D.R. helped with the abundance ratios. D.L., H.B.L. and K.Q. helped with discussions on magnetic fields. B.Z. helped with validating the distance measurements. L. Liu, G.L., C.-W.T., J. Wu and S.F. helped with discussions and in improving the paper. All authors reviewed the paper and were involved in discussions, telescope proposals and observations on which the raw data and the analyses were based.

Competing Interests Statement

The authors declare no competing interests.

References

1. Larson, R. B. Turbulence and star formation in molecular clouds. *Mon. Not. R. Astron. Soc.* **194**, 809–826 (1981).
2. Solomon, P. M., Rivolo, A. R., Barrett, J. & Yahil, A. Mass, Luminosity, and Line Width Relations of Galactic Molecular Clouds. *Astrophys. J.* **319**, 730 (1987).
3. Heyer, M., Krawczyk, C., Duval, J. & Jackson, J. M. Re-Examining Larson’s Scaling Relationships in Galactic Molecular Clouds. *Astrophys. J.* **699**, 1092–1103 (2009).
4. Miville-Deschênes, M.-A., Murray, N. & Lee, E. J. Physical Properties of Molecular Clouds for the Entire Milky Way Disk. *Astrophys. J.* **834**, 57 (2017).
5. Bolatto, A. D., Leroy, A. K., Rosolowsky, E., Walter, F. & Blitz, L. The Resolved Properties of Extragalactic Giant Molecular Clouds. *Astrophys. J.* **686**, 948–965 (2008).
6. Fukui, Y. & Kawamura, A. Molecular Clouds in Nearby Galaxies. *Annu. Rev. Astron. Astrophys.* **48**, 547–580 (2010).
7. Hughes, A. *et al.* Physical properties of giant molecular clouds in the Large Magellanic Cloud. *Mon. Not. R. Astron. Soc.* **406**, 2065–2086 (2010).
8. Schrubba, A. *et al.* Physical Properties of Molecular Clouds at 2 pc Resolution in the Low-metallicity Dwarf Galaxy NGC 6822 and the Milky Way. *Astrophys. J.* **835**, 278 (2017).
9. Wong, T. *et al.* Relations between Molecular Cloud Structure Sizes and Line Widths in the Large Magellanic Cloud. *Astrophys. J.* **885**, 50 (2019).
10. Saldaño, H. P. *et al.* CO(2–1) survey at 9 pc resolution in the Small Magellanic Cloud. *Astron. Astrophys.* **672**, A153 (2023).

11. Elmegreen, B. G. A Pressure and Metallicity Dependence for Molecular Cloud Correlations and the Calibration of Mass. *Astrophys. J.* **338**, 178 (1989).
12. Ballesteros-Paredes, J. Six myths on the virial theorem for interstellar clouds. *Mon. Not. R. Astron. Soc.* **372**, 443–449 (2006).
13. Bertoldi, F. & McKee, C. F. Pressure-confined Clumps in Magnetized Molecular Clouds. *Astrophys. J.* **395**, 140 (1992).
14. Sun, J. *et al.* Cloud-scale Molecular Gas Properties in 15 Nearby Galaxies. *Astrophys. J.* **860**, 172 (2018).
15. Federrath, C. *et al.* The Link between Turbulence, Magnetic Fields, Filaments, and Star Formation in the Central Molecular Zone Cloud G0.253+0.016. *Astrophys. J.* **832**, 143 (2016).
16. Liu, L. *et al.* WISDOM Project - IX. Giant molecular clouds in the lenticular galaxy NGC 4429: effects of shear and tidal forces on clouds. *Mon. Not. R. Astron. Soc.* **505**, 4048–4085 (2021).
17. Petkova, M. A. *et al.* Kinematics of Galactic Centre clouds shaped by shear-seeded solenoidal turbulence. *Mon. Not. R. Astron. Soc.* **525**, 962–968 (2023).
18. Bolatto, A. D., Wolfire, M. & Leroy, A. K. The CO-to-H₂ Conversion Factor. *Annu. Rev. Astron. Astrophys.* **51**, 207–268 (2013).
19. Swinbank, A. M. *et al.* The Interstellar Medium in Distant Star-forming Galaxies: Turbulent Pressure, Fragmentation, and Cloud Scaling Relations in a Dense Gas Disk at $z = 2.3$. *Astrophys. J.* **742**, 11 (2011).
20. McKee, C. F. & Tan, J. C. The Formation of Massive Stars from Turbulent Cores. *Astrophys. J.* **585**, 850–871 (2003).
21. Völschow, M., Banerjee, R. & Körtgen, B. Star formation in evolving molecular clouds. *Astron. Astrophys.* **605**, A97 (2017).
22. Hacar, A., Alves, J., Burkert, A. & Goldsmith, P. Opacity broadening and interpretation of suprathermal CO linewidths: Macroscopic turbulence and tangled molecular clouds. *Astron. Astrophys.* **591**, A104 (2016).
23. Wilson, T. L. & Rood, R. Abundances in the Interstellar Medium. *Annu. Rev. Astron. Astrophys.* **32**, 191–226 (1994).
24. Rathborne, J. M., Johnson, A. M., Jackson, J. M., Shah, R. Y. & Simon, R. Molecular Clouds and Clumps in the Boston University-Five College Radio Astronomy Observatory Galactic Ring Survey. *Astrophys. J.* **182**, 131–142 (2009).
25. Heyer, M. H., Carpenter, J. M. & Snell, R. L. The Equilibrium State of Molecular Regions in the Outer Galaxy. *Astrophys. J.* **551**, 852–866 (2001).
26. Benedettini, M. *et al.* Molecular cloud catalogue from ¹³CO (1-0) data of the Forgotten Quadrant Survey. *Astron. Astrophys.* **654**, A144 (2021).
27. Roman-Duval, J., Jackson, J. M., Heyer, M., Rathborne, J. & Simon, R. Physical Properties and Galactic Distribution of Molecular Clouds Identified in the Galactic Ring Survey. *Astrophys. J.* **723**, 492–507 (2010).
28. Rigby, A. J. *et al.* CHIMPS: physical properties of molecular clumps across the inner Galaxy. *Astron. Astrophys.* **632**, A58 (2019).

29. Knapen, J. H., Lee, J. C. & de Paz, A. G. *Outskirts of galaxies* (Springer, 2017).
30. Wolfire, M. G., McKee, C. F., Hollenbach, D. & Tielens, A. G. G. M. Neutral Atomic Phases of the Interstellar Medium in the Galaxy. *Astrophys. J.* **587**, 278–311 (2003).
31. Méndez-Delgado, J. E. *et al.* Gradients of chemical abundances in the Milky Way from H II regions: distances derived from Gaia EDR3 parallaxes and temperature inhomogeneities. *Mon. Not. R. Astron. Soc.* **510**, 4436–4455 (2022).
32. Chiappini, C. The chemical evolution of the galactic thick and thin disks. *Proceedings of the International Astronomical Union* **4**, 191–196 (2008).
33. Shi, Y. *et al.* Inefficient star formation in extremely metal poor galaxies. *Nature* **514**, 335–338 (2014).
34. Hunt, L. K. *et al.* ALMA observations of cool dust in a low-metallicity starburst, SBS 0335-052. *Astron. Astrophys.* **561**, A49 (2014).
35. Jacob, A. M. *et al.* First detection of ^{13}CH in the interstellar medium. *Astron. Astrophys.* **640**, A125 (2020).
36. Reid, M. J. *et al.* Trigonometric Parallaxes of High-mass Star-forming Regions: Our View of the Milky Way. *Astrophys. J.* **885**, 131 (2019).
37. Russell, S. C. & Dopita, M. A. Abundances of the Heavy Elements in the Magellanic Clouds. III. Interpretation of Results. *Astrophys. J.* **384**, 508 (1992).
38. Jameson, K. E. *et al.* First Results from the Herschel and ALMA Spectroscopic Surveys of the SMC: The Relationship between [C II]-bright Gas and CO-bright Gas at Low Metallicity. *Astrophys. J.* **853**, 111 (2018).
39. Pagel, B. E. J. CNO Abundances in Dwarf and Spiral Galaxies (invited review). In Charbonnel, C., Schaerer, D. & Meynet, G. (eds.) *CNO in the Universe*, vol. 304 of *Astronomical Society of the Pacific Conference Series*, 187 (2003).
40. García-Rojas, J., Peña, M., Flores-Durán, S. & Hernández-Martínez, L. The planetary nebulae and H II regions in NGC 6822 revisited. Clues to AGB nucleosynthesis. *Astron. Astrophys.* **586**, A59 (2016).
41. Shi, Y. *et al.* Oversized Gas Clumps in an Extremely Metal-poor Molecular Cloud Revealed by ALMA's Parsec-scale Maps. *Astrophys. J.* **892**, 147 (2020).
42. Ohno, T. *et al.* An Unbiased CO Survey Toward the Northern Region of the Small Magellanic Cloud with the Atacama Compact Array. II. CO Cloud Catalog. *Astrophys. J.* **949**, 63 (2023).
43. Spitzer Jr, L. *Physical processes in the interstellar medium* (John Wiley & Sons, 2008).
44. Williams, J. P., Bergin, E. A., Caselli, P., Myers, P. C. & Plume, R. The Ionization Fraction in Dense Molecular Gas. I. Low-Mass Cores. *Astrophys. J.* **503**, 689–699 (1998).
45. Crutcher, R. M., Wandelt, B., Heiles, C., Falgarone, E. & Troland, T. H. Magnetic Fields in Interstellar Clouds from Zeeman Observations: Inference of Total Field Strengths by Bayesian Analysis. *Astrophys. J.* **725**, 466–479 (2010).
46. Kobayashi, M. I. N. *et al.* Metallicity Dependence of Molecular Cloud Hierarchical Structure at Early Evolutionary Stages. *Astrophys. J.* **954**, 38 (2023).
47. Lequeux, J. *The interstellar medium* (Springer Science & Business Media, 2004).

48. Field, G. B., Blackman, E. G. & Keto, E. R. Does external pressure explain recent results for molecular clouds? *Mon. Not. R. Astron. Soc.* **416**, 710–714 (2011).
49. Ramírez-Galeano, L., Ballesteros-Paredes, J., Smith, R. J., Camacho, V. & Zamora-Avilés, M. Why most molecular clouds are gravitationally dominated. *Mon. Not. R. Astron. Soc.* **515**, 2822–2836 (2022).
50. Curtis-Lake, E. *et al.* Spectroscopic confirmation of four metal-poor galaxies at $z = 10.3$ – 13.2 . *Nature Astronomy* **7**, 622–632 (2023).
51. Wouterloot, J. G. A. & Brand, J. IRAS sources beyond the solar circle. I. CO observations. *Astron. Astrophys. Suppl.* **80**, 149–187 (1989).
52. Sun, Y. *et al.* A Possible Extension of the Scutum-Centaurus Arm into the Outer Second Quadrant. *Astrophys. J. Let.* **798**, L27 (2015).
53. Li, H.-K. *et al.* Oxygen isotopic ratios toward molecular clouds in the Galactic disk. *Research in Astronomy and Astrophysics* **16**, 47 (2016).
54. Sun, Y. *et al.* Molecular Clouds in the Extreme Outer Galaxy between $l = 34.^{\circ}75$ to $45.^{\circ}25$. *Astrophys. Js* **230**, 17 (2017).
55. Jackson, J. M. *et al.* The Boston University-Five College Radio Astronomy Observatory Galactic Ring Survey. *Astrophys. Js* **163**, 145–159 (2006).
56. Pietrzyński, G. *et al.* A distance to the Large Magellanic Cloud that is precise to one per cent. *Nature* **567**, 200–203 (2019).
57. Graczyk, D. *et al.* A Distance Determination to the Small Magellanic Cloud with an Accuracy of Better than Two Percent Based on Late-type Eclipsing Binary Stars. *Astrophys. J.* **904**, 13 (2020).
58. Rich, J. A. *et al.* A New Cepheid Distance Measurement and Method for NGC 6822. *Astrophys. J.* **794**, 107 (2014).
59. Whiting, M. T. DUCHAMP: a 3D source finder for spectral-line data. *Mon. Not. R. Astron. Soc.* **421**, 3242–3256 (2012).
60. Di Teodoro, E. M. & Fraternali, F. ^{3D} BAROLO: a new 3D algorithm to derive rotation curves of galaxies. *Mon. Not. R. Astron. Soc.* **451**, 3021–3033 (2015).
61. Mangum, J. G. & Shirley, Y. L. How to Calculate Molecular Column Density. *Publ. Astron. Soc. Pac.* **127**, 266 (2015).
62. Tang, X. D. *et al.* Kinetic temperature of massive star forming molecular clumps measured with formaldehyde. *Astron. Astrophys.* **598**, A30 (2017).
63. Chira, R. A. *et al.* Characterization of infrared dark clouds. NH₃ observations of an absorption-contrast selected IRDC sample. *Astron. Astrophys.* **552**, A40 (2013).
64. Fehér, O. *et al.* Ammonia Emission in Various Star-forming Environments: A Pilot Study of Planck Galactic Cold Clumps. *Astrophys. Js* **258**, 17 (2022).
65. Garden, R. P., Hayashi, M., Gatley, I., Hasegawa, T. & Kaifu, N. A Spectroscopic Study of the DR 21 Outflow Source. III. The CO Line Emission. *Astrophys. J.* **374**, 540 (1991).
66. Lacy, J. H., Sneden, C., Kim, H. & Jaffe, D. T. H₂, CO, and Dust Absorption through Cold Molecular Clouds. *Astrophys. J.* **838**, 66 (2017).

67. Fujii, K. *et al.* Dense Molecular Clumps Associated with the Large Magellanic Cloud Supergiant Shells LMC 4 and LMC 5. *Astrophys. J.* **796**, 123 (2014).
68. Condon, J. J. Errors in Elliptical Gaussian Fits. *Publ. Astron. Soc. Pac.* **109**, 166–172 (1997).
69. Mueller, K. E., Shirley, Y. L., Evans, I., Neal J. & Jacobson, H. R. The Physical Conditions for Massive Star Formation: Dust Continuum Maps and Modeling. *Astrophys. Js* **143**, 469–497 (2002).
70. Wouterloot, J. G. A. & Brand, J. IRAS sources beyond the solar circle. VII. The $\hat{I}2\hat{C}/\hat{I}3\hat{C}$ ratio in the far outer Galaxy. *Astron. Astrophys. Suppl.* **119**, 439–457 (1996).
71. Milam, S. N., Savage, C., Brewster, M. A., Ziurys, L. M. & Wyckoff, S. The $^{12}\text{C}/^{13}\text{C}$ Isotope Gradient Derived from Millimeter Transitions of CN: The Case for Galactic Chemical Evolution. *Astrophys. J.* **634**, 1126–1132 (2005).
72. Sun, Y. *et al.* An improved method to measure $^{12}\text{C}/^{13}\text{C}$ and $^{14}\text{N}/^{15}\text{N}$ abundance ratios: revisiting CN isotopologues in the Galactic outer disc. *Mon. Not. R. Astron. Soc.* **527**, 8151–8192 (2024).
73. Szűcs, L., Glover, S. C. O. & Klessen, R. S. The $^{12}\text{CO}/^{13}\text{CO}$ ratio in turbulent molecular clouds. *Mon. Not. R. Astron. Soc.* **445**, 4055–4072 (2014).
74. Dickman, R. L. The ratio of carbon monoxide to molecular hydrogen in interstellar dark clouds. *Astrophys. Js* **37**, 407–427 (1978).
75. Frerking, M. A., Langer, W. D. & Wilson, R. W. The relationship between carbon monoxide abundance and visual extinction in interstellar clouds. *Astrophys. J.* **262**, 590–605 (1982).
76. Romano, D., Matteucci, F., Zhang, Z.-Y., Ivison, R. J. & Ventura, P. The evolution of CNO isotopes: the impact of massive stellar rotators. *Mon. Not. R. Astron. Soc.* **490**, 2838–2854 (2019).
77. Glover, S. C. O. & Clark, P. C. Star formation in metal-poor gas clouds. *Mon. Not. R. Astron. Soc.* **426**, 377–388 (2012).
78. Kauffmann, J., Pillai, T. & Goldsmith, P. F. Low Virial Parameters in Molecular Clouds: Implications for High-mass Star Formation and Magnetic Fields. *Astrophys. J.* **779**, 185 (2013).
79. Meidt, S. E. *et al.* A Model for the Onset of Self-gravitation and Star Formation in Molecular Gas Governed by Galactic Forces. I. Cloud-scale Gas Motions. *Astrophys. J.* **854**, 100 (2018).
80. Zhang, Z.-Y. *et al.* Physical conditions of molecular gas in the Circinus galaxy Multi-J CO and C^3PP_0 observations. *Astron. Astrophys.* **568**, A122 (2014).
81. Papadopoulos, P. P. & Seaquist, E. R. The State of the Molecular Gas in a Luminous Starburst/Seyfert 2 Galaxy: NGC 1068 Revisited. *Astrophys. J.* **516**, 114–126 (1999).
82. Elmegreen, B. G. Magnetic diffusion and ionization fractions in dense molecular clouds: the role of charged grains. *Astrophys. J.* **232**, 729–739 (1979).
83. Padovani, M. On the origin of cosmic-ray ionisation in star-forming regions. In *Physics and Chemistry of Star Formation: The Dynamical ISM Across Time and Spatial Scales*, 237 (2023).
84. Crutcher, R. M. Magnetic Fields in Molecular Clouds. *Annu. Rev. Astron. Astrophys.* **50**, 29–63 (2012).
85. Ching, T. C. *et al.* An early transition to magnetic supercriticality in star formation. *Nature* **601**, 49–52 (2022).
86. Cao, Z. & Li, H.-b. Turbulence in Zeeman Measurements from Molecular Clouds. *Astrophys. J. Let.* **946**, L46 (2023).

87. Basu, A. & Roy, S. Magnetic fields in nearby normal galaxies: energy equipartition. *Mon. Not. R. Astron. Soc.* **433**, 1675–1686 (2013).
88. Beck, R. Magnetic fields in the nearby spiral galaxy IC 342: A multi-frequency radio polarization study. *Astron. Astrophys.* **578**, A93 (2015).
89. Li, D., Kauffmann, J., Zhang, Q. & Chen, W. Massive Quiescent Cores in Orion: Dynamical State Revealed by High-resolution Ammonia Maps. *Astrophys. J. Let.* **768**, L5 (2013).
90. Wang, K., Wang, Y. & Xu, F. Massive Star Formation Starts in Subvirial Dense Clumps Unless Resisted by Strong Magnetic Fields. *Astrophys. J. Let.* **974**, L6 (2024).
91. Koda, J., Sawada, T., Hasegawa, T. & Scoville, N. Z. The Elongations and Supersonic Motions of Molecular Clouds. *Astrophys. J.* **638**, 191–195 (2006).
92. Tan, J. C., Krumholz, M. R. & McKee, C. F. Equilibrium Star Cluster Formation. *Astrophys. J. Let.* **641**, L121–L124 (2006).
93. Padoan, P., Pan, L., Haugbølle, T. & Nordlund, Å. Supernova Driving. I. The Origin of Molecular Cloud Turbulence. *Astrophys. J.* **822**, 11 (2016).
94. Aouad, C. J., James, P. A. & Chilingarian, I. V. Coupling local to global star formation in spiral galaxies: the effect of differential rotation. *Mon. Not. R. Astron. Soc.* **496**, 5211–5226 (2020).
95. Lee, E. J., Miville-Deschênes, M.-A. & Murray, N. W. Observational Evidence of Dynamic Star Formation Rate in Milky Way Giant Molecular Clouds. *Astrophys. J.* **833**, 229 (2016).
96. Elia, D. *et al.* The Star Formation Rate of the Milky Way as Seen by Herschel. *Astrophys. J.* **941**, 162 (2022).
97. Lada, C. J. Star formation: from ob associations to protostars. In *Symposium-International astronomical union*, vol. 115, 1–18 (Cambridge University Press, 1987).
98. Hansen, C. E., Klein, R. I., McKee, C. F. & Fisher, R. T. Feedback Effects on Low-mass Star Formation. *Astrophys. J.* **747**, 22 (2012).
99. Li, H. *et al.* Outflows and Bubbles in Taurus: Star-formation Feedback Sufficient to Maintain Turbulence. *Astrophys. Js* **219**, 20 (2015).
100. Sun, Y. *et al.* Discovery of H₂O, CH₃OH, and OH Masers in the Extreme Outer Galaxy. *Astrophys. J.* **869**, 148 (2018).
101. Shirley, Y. L. The Critical Density and the Effective Excitation Density of Commonly Observed Molecular Dense Gas Tracers. *Publ. Astron. Soc. Pac.* **127**, 299 (2015).
102. Carilli, C. L. & Walter, F. Cool Gas in High-Redshift Galaxies. *Annu. Rev. Astron. Astrophys.* **51**, 105–161 (2013).
103. Draine, B. T. *Physics of the interstellar and intergalactic medium*, vol. 19 (Princeton University Press, 2010).
104. Oka, T. *et al.* Statistical Properties of Molecular Clouds in the Galactic Center. *Astrophys. J.* **562**, 348–362 (2001).
105. Lin, L. Dataset for the paper — Inadequate turbulent support in low-metallicity molecular clouds. *figshare* <https://doi.org/10.6084/m9.figshare.27282924> (2024).
106. Jiao, Y. *et al.* Detection of the Keplerian decline in the Milky Way rotation curve. *Astron. Astrophys.* **678**, A208 (2023).

Supplementary Table 2: Measured quantities for molecular clouds observed by IRAM 30-m and SMT.

*: Clouds with strong VLASS or NVSS continuum.

Target	l ($^{\circ}$)	b ($^{\circ}$)	V_{LSR} (km s^{-1})	R_{gc} (kpc)	d (kpc)	R_{cloud} (pc)	σ_v (km s^{-1})	M_{cloud} ($10^3 M_{\odot}$)	n_{H_2} (10^4 cm^{-3})	α_{vir}
IRAM 30-m (2016)										
G37.350	37.35	1.06	-54.0	13.2 \pm 1	18.7 \pm 1	1.0 \pm 0.1	0.9 \pm 0.09	1.1 \pm 0.2	0.3	1.0 \pm 0.3
G44.8	44.80	0.66	-61.9	13.0 \pm 1	17.5 \pm 1	0.9 \pm 0.1	1.0 \pm 0.1	0.9 \pm 0.2	0.5	1.1 \pm 0.3
IRAS0245	136.35	0.96	-61.5	13.2 \pm 1	6.0 \pm 1	0.4 \pm 0.08	0.7 \pm 0.07	0.4 \pm 0.07	2	0.7 \pm 0.3
SUN15_14N	109.29	2.08	-101.1	14.9 \pm 1	10.1 \pm 1	0.9 \pm 0.1	0.5 \pm 0.05	0.4 \pm 0.08	0.2	0.7 \pm 0.2
SUN15_18	109.79	2.71	-99.1	14.7 \pm 0.9	9.8 \pm 1	0.7 \pm 0.1	0.4 \pm 0.04	0.3 \pm 0.07	0.4	0.4 \pm 0.1
SUN15_21*	114.34	0.79	-101.0	15.4 \pm 1	10.1 \pm 1	1.4 \pm 0.2	0.5 \pm 0.05	0.8 \pm 0.2	0.1	0.6 \pm 0.2
SUN15_34	122.77	2.52	-107.0	17.8 \pm 2	12.0 \pm 2	1.1 \pm 0.2	0.5 \pm 0.05	0.8 \pm 0.2	0.2	0.4 \pm 0.1
SUN15_56	137.77	-0.97	-103.1	24.1 \pm 4	17.4 \pm 4	2.7 \pm 0.6	0.7 \pm 0.07	13.6 \pm 3	0.3	0.1 \pm 0.04
SUN15_57	137.78	-1.07	-102.2	23.7 \pm 3	17.0 \pm 4	1.4 \pm 0.3	0.6 \pm 0.06	3.2 \pm 0.6	0.4	0.2 \pm 0.07
SUN15_7W	104.98	3.31	-102.6	14.8 \pm 0.9	10.5 \pm 1	0.7 \pm 0.1	0.6 \pm 0.06	0.3 \pm 0.07	0.4	0.9 \pm 0.3
WB89_380*	124.65	2.54	-86.2	14.7 \pm 1	8.5 \pm 1	1.1 \pm 0.2	1.4 \pm 0.1	2.2 \pm 0.4	0.5	1.2 \pm 0.4
WB89_391*	125.80	3.05	-86.1	14.9 \pm 1	8.6 \pm 1	0.5 \pm 0.09	0.7 \pm 0.07	0.4 \pm 0.08	1	0.7 \pm 0.2
WB89_437	135.28	2.80	-71.8	13.4 \pm 0.6	6.3 \pm 0.6	0.5 \pm 0.07	1.2 \pm 0.1	0.5 \pm 0.1	1	1.5 \pm 0.5
WB89_501	145.20	2.98	-58.2	14.6 \pm 1	7.1 \pm 2	0.3 \pm 0.07	0.8 \pm 0.08	0.3 \pm 0.07	4	0.7 \pm 0.3
IRAM 30-m (2023)										
SUN15_23	116.72	3.54	-107.2	16.6 \pm 1	11.3 \pm 1	0.7 \pm 0.1	0.6 \pm 0.06	0.4 \pm 0.07	0.4	0.8 \pm 0.3
SUN15_25	117.58	3.95	-106.0	16.6 \pm 1	11.2 \pm 1	0.3 \pm 0.05	0.5 \pm 0.05	0.2 \pm 0.04	2	0.5 \pm 0.2
SUN15_30	121.81	3.05	-104.1	17.0 \pm 1	11.3 \pm 2	0.8 \pm 0.1	0.6 \pm 0.06	0.5 \pm 0.1	0.3	0.7 \pm 0.2
SUN15_53	137.29	-1.16	-101.5	23.0 \pm 3	16.3 \pm 3	2.3 \pm 0.5	0.5 \pm 0.05	1.4 \pm 0.3	0.04	0.4 \pm 0.2
SUN15_55	137.62	-1.23	-98.8	22.1 \pm 3	15.4 \pm 3	1.1 \pm 0.2	0.5 \pm 0.05	0.9 \pm 0.2	0.2	0.4 \pm 0.1
SUN15_59	139.12	-1.47	-96.6	22.4 \pm 3	15.6 \pm 3	0.5 \pm 0.1	0.4 \pm 0.04	0.5 \pm 0.1	1	0.2 \pm 0.06
SUN15_69	145.21	-0.39	-74.0	18.5 \pm 2	11.2 \pm 2	1.2 \pm 0.3	0.5 \pm 0.05	0.4 \pm 0.08	0.08	0.8 \pm 0.3
SUN15_72	146.06	-1.65	-77.4	20.3 \pm 3	13.1 \pm 3	1.9 \pm 0.5	0.5 \pm 0.05	0.9 \pm 0.2	0.05	0.6 \pm 0.2
SMT (2022)										
SUN15_47	131.16	1.39	-100.4	19.0 \pm 2	12.6 \pm 2	0.2 \pm 0.03	0.3 \pm 0.03	0.1 \pm 0.03	8	0.2 \pm 0.06
WB89_379	124.56	2.52	-88.1	15.0 \pm 1	8.8 \pm 1	0.5 \pm 0.09	0.9 \pm 0.09	0.3 \pm 0.07	0.9	1.5 \pm 0.5
WB89_434	135.99	0.67	-78.0	15.7 \pm 1	8.8 \pm 2	0.5 \pm 0.09	0.5 \pm 0.05	0.1 \pm 0.01	0.3	2.0 \pm 0.7
WB89_365	123.07	1.35	-90.9	15.1 \pm 1	9.1 \pm 1	0.5 \pm 0.08	0.5 \pm 0.05	0.1 \pm 0.01	0.2	2.6 \pm 0.8

Supplementary Table 3: Measured quantities for molecular clouds observed by ALMA Total Power.

*: Clouds with strong VLASS or NVSS continuum. †: Clouds outside of the sky coverage of VLA.

Target	l ($^{\circ}$)	b ($^{\circ}$)	V_{LSR} (km s^{-1})	R_{gc} (kpc)	d (kpc)	R_{cloud} (pc)	σ_v (km s^{-1})	M_{cloud} ($10^3 M_{\odot}$)	n_{H_2} (10^4 cm^{-3})	α_{vir}
ALMA Total Power (Cycle 8)										
WB89_766	193.43	-1.17	22.3	14.4 \pm 3	6.4 \pm 3	0.6 \pm 0.3	1.1 \pm 0.1	0.4 \pm 0.07	0.5	2.3 \pm 1
WB89_770*	192.91	-0.63	22.6	15.0 \pm 3	7.0 \pm 3	0.4 \pm 0.2	0.9 \pm 0.09	0.3 \pm 0.07	3	1.0 \pm 0.5
WB89_1086	245.93	1.17	63.5	11.6 \pm 0.6	5.6 \pm 0.8	0.8 \pm 0.1	0.7 \pm 0.07	0.3 \pm 0.06	0.2	1.8 \pm 0.6
WB89_765*	196.83	-3.11	25.7	12.2 \pm 0.2	4.1 \pm 0.2	0.4 \pm 0.05	0.8 \pm 0.08	0.2 \pm 0.05	1	1.5 \pm 0.5
WB89_771	193.69	-1.06	22.9	14.5 \pm 3	6.4 \pm 3	0.7 \pm 0.3	0.9 \pm 0.09	0.2 \pm 0.04	0.3	2.7 \pm 1
WB89_1010	230.55	1.92	63.1	11.7 \pm 0.3	4.7 \pm 0.3	0.4 \pm 0.04	0.6 \pm 0.06	0.1 \pm 0.02	0.5	2.1 \pm 0.6
WB89_1049*	241.54	-0.60	70.5	11.9 \pm 0.4	5.6 \pm 0.5	0.9 \pm 0.1	0.8 \pm 0.08	0.3 \pm 0.07	0.2	1.9 \pm 0.6
WB89_1048*	240.32	0.07	67.8	11.9 \pm 0.4	5.5 \pm 0.5	0.4 \pm 0.06	2.4 \pm 0.2	0.4 \pm 0.09	2	6.5 \pm 2
WB89_1158†	260.69	-1.39	66.3	11.5 \pm 0.5	6.8 \pm 0.8	1.0 \pm 0.2	1.2 \pm 0.1	0.4 \pm 0.09	0.1	3.8 \pm 1
WB89_782*	196.46	-1.68	17.1	12.2 \pm 0.2	4.1 \pm 0.2	0.6 \pm 0.07	1.5 \pm 0.2	0.7 \pm 0.1	1	2.3 \pm 0.7
WB89_959	231.52	-4.30	52.9	11.5 \pm 0.7	4.5 \pm 0.8	0.6 \pm 0.1	1.0 \pm 0.1	0.2 \pm 0.04	0.3	3.5 \pm 1
WB89_886	212.06	-0.74	44.6	11.9 \pm 0.2	4.2 \pm 0.2	0.3 \pm 0.04	1.6 \pm 0.2	0.1 \pm 0.03	1	7.4 \pm 2
WB89_905	211.59	1.06	44.8	11.9 \pm 0.2	4.2 \pm 0.2	0.4 \pm 0.04	1.6 \pm 0.2	0.2 \pm 0.04	1	5.7 \pm 2
WB89_1236†	269.22	-0.31	74.8	12.0 \pm 0.6	8.7 \pm 0.8	0.8 \pm 0.1	0.7 \pm 0.07	0.2 \pm 0.04	0.1	2.2 \pm 0.7
WB89_762	190.97	-0.06	11.0	11.1 \pm 3	3.0 \pm 3	0.5 \pm 0.5	0.5 \pm 0.05	0.1 \pm 0.01	0.2	2.1 \pm 2
WB89_904	211.04	1.18	55.2	15.0 \pm 2	7.4 \pm 2	1.1 \pm 0.3	0.8 \pm 0.08	0.6 \pm 0.1	0.1	1.6 \pm 0.6
WB89_864	210.24	-1.33	37.0	12.0 \pm 1	4.2 \pm 1	0.3 \pm 0.09	0.8 \pm 0.08	0.0 \pm 0.01	0.6	4.7 \pm 2
WB89_985N	229.57	0.15	53.2	11.6 \pm 0.2	4.6 \pm 0.3	0.5 \pm 0.06	1.4 \pm 0.1	0.2 \pm 0.05	0.6	4.9 \pm 2
WB89_985S	229.57	0.15	53.2	11.6 \pm 0.2	4.6 \pm 0.3	0.5 \pm 0.06	1.0 \pm 0.1	0.2 \pm 0.04	0.5	3.0 \pm 0.9
WB89_885	212.35	-0.92	44.3	11.9 \pm 0.2	4.2 \pm 0.2	0.8 \pm 0.09	1.2 \pm 0.1	0.3 \pm 0.06	0.2	4.3 \pm 1
WB89_1145†	259.24	-1.63	62.7	11.2 \pm 0.5	6.4 \pm 0.8	0.3 \pm 0.05	0.7 \pm 0.07	0.0 \pm 0.01	0.5	4.1 \pm 1
WB89_1245†	269.85	-0.06	74.4	12.0 \pm 0.6	8.7 \pm 0.8	0.9 \pm 0.1	1.6 \pm 0.2	0.7 \pm 0.1	0.3	4.0 \pm 1
WB89_920	215.19	0.81	48.7	12.8 \pm 1	5.2 \pm 1	0.9 \pm 0.2	0.8 \pm 0.08	0.4 \pm 0.08	0.2	1.8 \pm 0.7
WB89_1057	242.94	-0.45	63.6	11.7 \pm 0.6	5.5 \pm 0.8	0.6 \pm 0.1	1.6 \pm 0.2	0.2 \pm 0.04	0.3	8.8 \pm 3
WB89_758	193.31	-1.45	28.7	18.5 \pm 4	10.5 \pm 4	0.7 \pm 0.3	0.7 \pm 0.07	0.3 \pm 0.07	0.3	1.2 \pm 0.6
WB89_916	212.96	1.30	42.4	11.9 \pm 0.2	4.2 \pm 0.2	0.8 \pm 0.09	0.9 \pm 0.09	0.2 \pm 0.05	0.2	2.9 \pm 0.9